

## Micro-optical devices for fiber communication

**Citation for published version (APA):**

Nicia, A. J. A. (1983). *Micro-optical devices for fiber communication*. [Phd Thesis 1 (Research TU/e / Graduation TU/e), Electrical Engineering]. Technische Hogeschool Eindhoven. <https://doi.org/10.6100/IR98182>

**DOI:**

[10.6100/IR98182](https://doi.org/10.6100/IR98182)

**Document status and date:**

Published: 01/01/1983

**Document Version:**

Publisher's PDF, also known as Version of Record (includes final page, issue and volume numbers)

**Please check the document version of this publication:**

- A submitted manuscript is the version of the article upon submission and before peer-review. There can be important differences between the submitted version and the official published version of record. People interested in the research are advised to contact the author for the final version of the publication, or visit the DOI to the publisher's website.
- The final author version and the galley proof are versions of the publication after peer review.
- The final published version features the final layout of the paper including the volume, issue and page numbers.

[Link to publication](#)

**General rights**

Copyright and moral rights for the publications made accessible in the public portal are retained by the authors and/or other copyright owners and it is a condition of accessing publications that users recognise and abide by the legal requirements associated with these rights.

- Users may download and print one copy of any publication from the public portal for the purpose of private study or research.
- You may not further distribute the material or use it for any profit-making activity or commercial gain
- You may freely distribute the URL identifying the publication in the public portal.

If the publication is distributed under the terms of Article 25fa of the Dutch Copyright Act, indicated by the "Taverne" license above, please follow below link for the End User Agreement:

[www.tue.nl/taverne](http://www.tue.nl/taverne)

**Take down policy**

If you believe that this document breaches copyright please contact us at:

[openaccess@tue.nl](mailto:openaccess@tue.nl)

providing details and we will investigate your claim.

**MICRO-OPTICAL DEVICES FOR  
FIBER COMMUNICATION**

**A. J. A. NICIA**

# **MICRO-OPTICAL DEVICES FOR FIBER COMMUNICATION**

*aan Hilda*

# **MICRO-OPTICAL DEVICES FOR FIBER COMMUNICATION**

**PROEFSCHRIFT**

**TER VERKRIJGING VAN DE GRAAD VAN  
DOCTOR IN DE TECHNISCHE WETENSCHAPPEN  
AAN DE TECHNISCHE HOGESCHOOL EINDHOVEN,  
OP GEZAG VAN DE RECTOR MAGNIFICUS,  
PROF. DR. S.T.M. ACKERMANS, VOOR EEN COMMISSIE  
AANGEWENZEN DOOR HET COLLEGE VAN DEKANEN  
IN HET OPENBAAR TE VERDEDIGEN  
OP VRIJDAG 10 JUNI 1983 TE 16.00 UUR**

**DOOR**

**ANTONIUS JOSEPHUS ADRIANUS NICIA**

**geboren te Breda**



**DIT PROEFSCHRIFT IS GOEDGEKEURD  
DOOR DE PROMOTOREN**

**Prof. ir. J. van der Plaats**

**en**

**Prof. dr. G.A. Acket**

**Nicia, Antonius Josephus Adrianus**

**Micro-optic devices for fiber communication /  
Antonius Josephus Adrianus Nicia. — [S.l. : s.n.]. —  
Fig. — Proefschrift Eindhoven. — Met lit. opg., reg.  
ISBN 90-9000441-6  
SISO 668.2 UDC 621.372.8:621.315.612 UGI 650  
Trefw.: optische communicatie.**

## PREFACE

Optical fiber communication has many outstanding advantages. Its potentially wide application ranges from long-distance trunk lines to short-distance subscriber networks. This is mainly due to the favorable features of optical fibers, notably low loss, wide bandwidth, freedom from electromagnetic interference, light weight and small dimensions. To fully utilize these advantages and to further expand the application areas, various micro-optical devices are required in addition to those included in the basic optical link (source-fiber-detector).

Among micro-optical devices optical multiplexers and demultiplexers are probably the most important ones, because they allow wavelength division multiplexing (WDM) at a single fiber. WDM, in particular, makes optical fiber communication attractive for subscriber and data networks owing to the system flexibility thus introduced. Most of these devices include a lens coupling between a source fiber and a receiving fiber. The minimum insertion loss of such a coupling is completely determined by the aberrations of the incorporated lenses.

This thesis develops the relationship between optical aberrations and coupling efficiency for multimode fiber devices. Results of this lens-coupling investigation are applied in the design of those optical multiplexers and demultiplexers intended for WDM transmission, that contain lenses. In addition, the system requirements to be met by multiplexers and demultiplexers are studied to facilitate the choice of proper input and output fibers for these devices.

Most of the work presented here has been published before in:

1. Lens Coupling in Fiber-Optic Devices: Efficiency Limits  
A. Nicia, Appl. Opt. 20, 3136 (1981).
2. Wavelength Multiplexing and Demultiplexing Systems for Single-Mode and Multimode Fibers  
A. Nicia, in Technical Digest, Seventh ECOC, Copenhagen (1981), p. 8.1-1.
3. Loss Analysis of Laser-Fiber Coupling and Fiber Combiner and its Application to Wavelength Division Multiplexing  
A. Nicia, Appl. Opt. 21, 4280 (1982).

With respect to notation, little or no attempt has been made to retain uniform symbols throughout the thesis. For example,  $L$  is used in one chapter as the radiance and elsewhere as one of the optical direction cosines. However, a perceptive reader should have no difficulty with changes of this kind.

**ACKNOWLEDGEMENT**

The research reported in this thesis has been performed at Philips Research Laboratories, Eindhoven, The Netherlands.

The author expresses his gratitude to the management of this Laboratory for their permission to publish this thesis. Thanks are also due to all the members of the *Wide Band Communication Group*, particularly to Mr. A. van de Grijp, Mr. G.D. Khoe, Mr. J.A. van Steenwijk and Mr. A.H.L. Tholen for their valuable cooperation. The author is especially indebted to Mr. C.J.T. Potters, Mr. D. Rittich and Mr. H.G. Finke for their most competent technical advice and experimental assistance.

Philips Research Laboratories  
Eindhoven, February 1983

A.J.A. Nicia

## TABLE OF CONTENTS

<b>1</b>	<b>LENS COUPLING IN FIBER-OPTICAL DEVICES</b>	<b>1</b>
1.1	Introduction	1
1.2	Paraxial Lens Characteristics	2
1.3	Spherical Aberration of the Lens System	4
1.4	Coupling Efficiency	8
1.5	Sensitivity to Mismatches	14
1.6	Experimental Results	19
	Appendix A	22
	Appendix B	23
	References	26
<b>2</b>	<b>GENERAL CONSIDERATIONS FOR WAVELENGTH DIVISION MULTIPLEXING</b>	<b>27</b>
2.1	Introduction	27
2.2	Optical Multiplexers	28
2.3	Optical Demultiplexers	30
2.4	External Conditions for Multi/Demultiplexers	34
2.4.1	Laser-Fiber Coupling	34
2.4.2	Lens Coupling between Unequal Fibers	47
	Appendix C	49
	References	50
<b>3</b>	<b>DESIGN AND CONSTRUCTION OF MULTIPLEXERS</b>	<b>51</b>
3.1	Introduction	51
3.2	Butt-Joint Multiplexer	51
3.2.1	Theory according to the Intensity Law	51
3.2.2	Theory according to Ray-Tracing	54
3.2.3	Overall Transmitter End Loss of a WDM System	63
3.2.4	Experimental Results	66
3.3	Prism Multiplexer	68
3.3.1	Theory	68
3.3.2	Design	69
3.3.3	Experimental Results	71
	References	73
<b>4</b>	<b>DESIGN AND CONSTRUCTION OF OPTICAL DEMULTIPLEXERS</b>	<b>74</b>
4.1	Introduction	74
4.2	Ball Lens Demultiplexer	74
4.2.1	Theory	74
4.2.2	Experimental Results	77
4.3	Linear Polarization Demultiplexer	80
	References	82
	SUMMARY AND CONCLUSIONS	83
	SAMENVATTING EN CONCLUSIES	84
	CURRICULUM VITAE	85

## 1. LENS COUPLING IN FIBER-OPTICAL DEVICES

### 1.1 Introduction

Fiber-optical communication systems that fully utilize the possibilities of optical fibers use components such as connectors, branch couplers, attenuators, switches, isolators and optical (de)multiplexers. To process or manipulate the light between fibers at least several millimeters are needed between the endfaces for inserting the processing element, which can be an interference filter, a grating, etc. Due to the large divergence of the light radiated by fibers (typically  $24^\circ$ ) such separations would lead to unacceptable insertion losses. This problem can be avoided by using a lens system between the fiber ends. Many such structures have been reported. In all of them a 1-1 image of the emitting fiber core is made upon the receiving one, while the light passes en route to the optical processing element. Coupling efficiency is now limited by lens aberrations. As the influence of grating efficiencies or transmission of interference filters etc. on the insertion loss of fiber-optical devices is quite well understood, the only remaining uncertain factor is the aberration loss. A recent paper contained some work on the numerical evaluation of the aberration loss of one specific configuration using GRIN-rod lenses [1]. However, so far no systematic approach has been presented, which results in a prediction of the coupling efficiency for a specified set of lens and fiber parameters. It is the aim of this treatise to remove this deficiency.

From our study and experiments, presented here, it follows that homogeneous single-element lenses and equivalent GRIN-rod lenses cause almost the same aberration loss. For a well-designed lens this results in a coupling efficiency of 95% (0.2 dB insertion loss) in the case of typical communication fibers.

The basic structure appearing in most devices is shown in Fig. 1.1. It is a centered optical system with a collimating and a focusing lens. (The optical processing elements are always omitted in the figures.) Some devices use off-axis fiber ends.

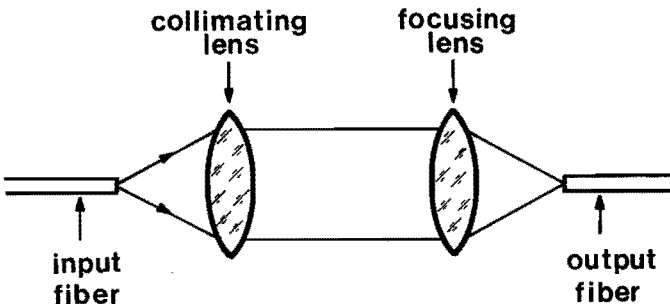


*Fig. 1.1 Basic structure of lens coupling*

Since the spherical aberration is dominant [2], in these devices too there is no loss of generality if we only consider the centered system. Another advantage of this lens coupling configuration is the possibility of using angular-dispersive elements, because of the collimated beam between the lenses [3].

Three types of single-element lenses for fiber-optical devices have been proposed: (1) quarter-pitch GRIN-rod lens [4], (2) ball lens [5], (3) rod lens [6]. The paraxial characteristics of the lens system and of each lens type are reviewed in Sec. 1.2. Their spherical aberration is studied in Sec. 1.3 and a detailed description of aberration loss is presented in Sec. 1.4. Discussions of the sensitivity to mismatches in Sec. 1.5 and experimental results in Sec. 1.6 complete the picture of lens coupling.

## 1.2 Paraxial Lens Characteristics

For a paraxial description of the lens system it is sufficient to represent the lenses in terms of their principal planes and focal points.

### A. GRIN-Rod Lens

The refractive index in a GRIN-rod lens is given by [7].

$$n(r) = n_0 [1 - (gr)^2 + h_4 (gr)^4 + h_6 (gr)^6]^{1/2}, \quad (1.1)$$

where

- $n(r)$  = refractive index at distance  $r$  from the axis,
- $n_0$  = refractive index on the axis,
- $g$  = focusing constant,
- $h_4, h_6$  = higher order constants.

For paraxial rays the higher order terms with coefficients  $h_4, h_6$  can be neglected. A meridional ray incident on a GRIN-rod lens travels along a sinusoidal curve with a periodic length [8], pitch,  $2\pi/g$ . For the usual quarter-pitch lens the focal length  $f$ , and the position of the principal points  $H$  are [8] (see Fig. 1.2a)

$$f = 1/n_0 g, \quad (1.2)$$

$$h = 1/n_0 g. \quad (1.3)$$

### B. Ball Lens

A ball lens is completely described by its refractive index  $n$  and radius  $R$ . Application of the thick lens formula [9] leads to (Fig. 1.2b)

$$f = \frac{n}{2(n-1)} R, \quad (1.4)$$

$$h = R. \quad (1.5)$$

### C. Rod Lens

One focal point of the rod lens is chosen at the plane face of the lens, so the only independent parameters are the refractive index  $n$  and radius of curvature  $R$  (Fig. 1.2c). Using the thick lens formula we get

$$f = \frac{1}{n-1}R, \quad (1.6)$$

$$h = \frac{1}{n-1}R. \quad (1.7)$$

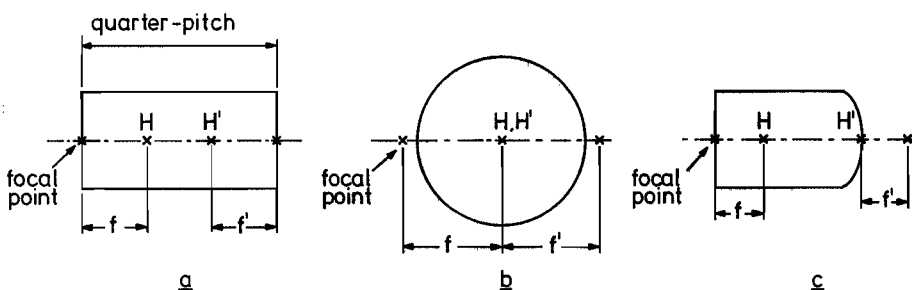


Fig. 1.2 Fundamental imaging parameters of the (a) GRIN-rod lens, (b) ball lens, (c) rod lens

### D. Complete Lens System

In lens connectors it is required that all assemblies containing one lens and one fiber end be identical in order to be interchangeable. For a maximum coupling between the fibers a 1-1 image should be made of the emitting fiber core upon the receiving one, and the launching angle with the fiber endface has to be the same at the receiving fiber end. All these conditions are satisfied only if the ends are positioned in the focal plane, while the foci of the lenses coincide (Fig. 1.3).

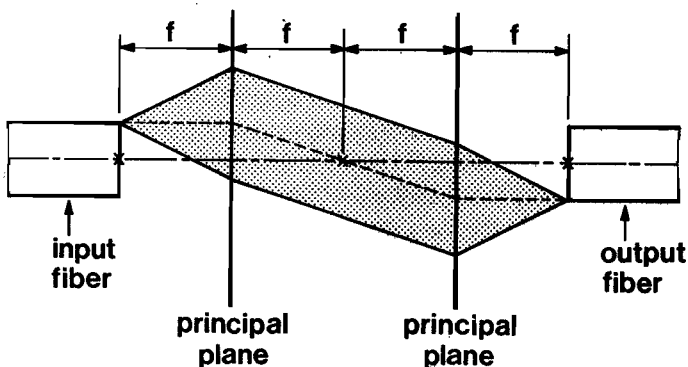


Fig. 1.3 Universal arrangement for optimal lens coupling



The incoming light cone is tilted if the foci of the lenses do not coincide. In a proper design this tilt angle should always be small compared with the numerical aperture of the fiber. Some applications allow the use of oversized output fibers for reducing the losses [10]. This aspect will be discussed in Sec. 2.4.2.

### 1.3 Spherical Aberration of the Lens System

We shall now investigate the spherical aberration of the lens system given in Fig. 1.3 when the above-mentioned types of lenses are inserted. As suggested in Fig. 1.4, the spherical aberration is the distance in the receiving focal plane between focused rays emitted at vanishing angles and at the outer region of the numerical aperture of the fiber.

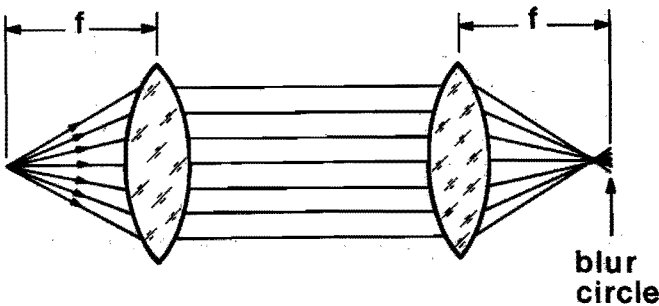


Fig. 1.4 The effect of spherical aberration

#### A. GRIN-Rod Lens

A lens with a sech distribution for  $n$  would not suffer from spherical aberration [11]. This requires that  $h_4$  and  $h_6$  in Eq. (1.1) equal  $2/3$  and  $-17/45$  respectively. However, as most GRIN-rod lenses are produced by means of ion-exchange techniques, the range of profiles is limited [12]. Although the diffusion and thus the profile can be influenced by applying electric fields [13], this method has not yet resulted in a good control of  $h_4$  and  $h_6$ . At present, therefore, most available GRIN-rod lenses are best described by parabolic distributions, i.e.

$$n(r) = n_0 [1 - (gr)^2]^{1/2}. \quad (1.8)$$

In Sec. 1.2 we point out that the focal points of the two lenses should coincide. As these points are at the flat planes of the lens, the complete lens system is equivalent to one half-pitch lens. Application of third-order aberration theory (see Appendix A) leads to

$$\epsilon = \frac{\pi}{2} \frac{1}{n_0^2} f NA^3, \quad (1.9)$$

where

- $\epsilon$  = radius of aberration circle,
- $n_0$  = on-axis refractive index,
- NA = numerical aperture of the fiber,
- $f$  = focal length, given by Eq. (1.2),

### *B. Ball Lens*

In Appendix B we use third-order aberration theory for deriving an expression for the spherical aberration of the ball lens system. The result is

$$\epsilon = \frac{1}{4} \left[ \frac{n}{(n-1)^2} - 1 \right] f NA^3, \quad (1.10)$$

where

- $\epsilon$  = radius of aberration circle,
- $n$  = refractive index of the ball lens,
- NA = numerical aperture of the fiber,
- $f$  = focal length, given by Eq. (1.4).

### *C. Rod Lens*

Following the same path given in Appendix B, one can derive for the rod lens system

$$\epsilon = \frac{1}{n^2(n-1)^2} f NA^3, \quad (1.11)$$

where

- $\epsilon$  = radius of aberration circle,
- $n$  = refractive index of the rod lens,
- NA = numerical aperture of the fiber,
- $f$  = focal length, given by Eq. (1.6).

#### D. General Considerations

Since the focal length in all fiber-optical devices is very large with respect to the fiber core dimensions, other lens aberrations have a negligible influence. The quality of the imaging is thus fully determined by the spherical aberration. This statement has been confirmed by exact ray-tracing, and was also established in some other work [2].

In an optical communication system the fiber parameters are determined by the required coupled input power, bit rate etc. On the other hand, the minimum focal length  $f$  in fiber-optical devices is determined by requirements of the width  $2.f.NA$  of the collimated beam, and/or its divergence  $2.a/f$  ( $a$  = fiber core radius). For a realistic comparison of the three lens types we therefore have to take equal focal lengths and use the lenses at equal numerical apertures, as both are prescribed by system demands regardless of lens type. Keeping this in mind we then see from Eqs. (1.9) – (1.11) that the characteristic aberration parameter  $\epsilon/fNA^3$  depends only on the refractive index. Fig. 1.5 shows a plot of  $\epsilon/fNA^3$  as a function of refractive index, making use of Eqs. (1.9) – (1.11). From Fig. 1.5 we see that, choosing  $n, n_0 > 1.75$ , we have almost equal imaging qualities for each type. Commercially available GRIN-rod lenses [14] have  $n_0 \cong 1.55$ . On the other hand, there is a wide range of optical glasses available for producing high-quality homogeneous lenses [15], with an upper limit  $n \cong 1.9$ .

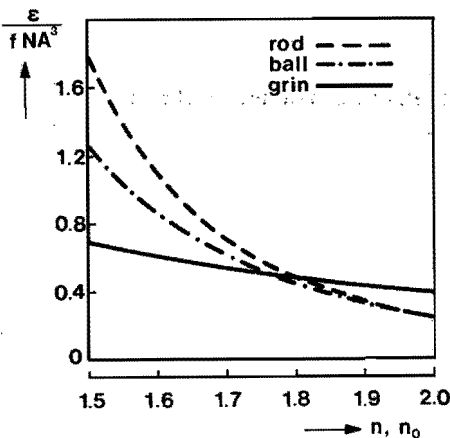


Fig. 1.5 Influence of material refractive index on the characteristic transverse spherical aberration of the lens coupling system.

Typical communication fibers have  $NA = 0.2$ , whereas in most fiber-optical devices the focal length is  $\sim 3$  mm. For these parameters the spherical aberration causes a blur circle with  $31 \mu\text{m}$  diam if use is made of a GRIN-rod lens ( $n_0 = 1.55$ ). This blur circle has a  $16 \mu\text{m}$  diam in the case of a ball lens or rod lens ( $n = 1.9$ ). These blur circles are certainly not small in comparison with the usual fiber core dimensions of  $50 \mu\text{m}$ . From Appendices A and B it follows that rays launched at nonvanishing angles cross the optical axis before the focal point. If the emitting point source and the receiving plane are at a distance  $f-z$  from the principal plane, where  $|z| \ll f$ , the paraxial image will be at  $f+z$  and thus at a distance  $2z$  behind the receiving plane. These considerations suggest that when the fiber ends are placed at a distance slightly smaller than the paraxial focal length, the spherical aberration may be partially compensated by a virtual negative endface separation between the image of the transmitting fiber and the receiving fiber.

Let us see how this defocusing affects the imaging of the ball lens system. The virtual separation causes a blur circle with radius  $2|z|.NA$ . (For the two other lens types the refractive index of the embedding medium should be taken into account.) Using this effect and Eq. (1.10) we get a more general expression for the place where the refocused rays arrive at the receiving plane:

$$e(\theta) = -2z\theta + \frac{1}{4} \left[ \frac{n}{(n-1)^2} - 1 \right] f \theta^3, \quad (1.12)$$

in which

- $e(\theta)$  = distance to the optical axis where refocused rays arrive at the receiving plane, positive if rays cross the axis before this plane,
- $\theta$  = launching angle,
- $z$  = defocusing, positive if the fiber ends are at distances shorter than the focal length.

Note that Eq. (1.12) concerns one single ray launched at an angle  $\theta$ .

The effect of defocusing is shown in Fig. 1.6. The solid curves were obtained by means of exact ray-tracing, the dashed ones with the aid of Eq. (1.12). The parameters of the ball lenses which we used in our experiments were taken for Fig. 1.6a, and for Fig. 1.6b we used a ball lens with low refractive index. It can be seen that the spherical aberration can be remarkably reduced by this defocusing. How far the defocusing has to go for optimal coupling will be discussed in the next section. Studying Fig. 1.6 we also see that third-order aberration theory gives a satisfactory description of all cases of interest. For GRIN-rod lenses and rod lenses this defocusing means that the lens thickness should be slightly less than a quarter-pitch or the paraxial focal length, respectively.

Without presenting the relations explicitly, it will be clear that in the case of GRIN-rod lens or rod lens, Eq. (1.12) has exactly the same form.

Finally we note that the diffraction limit (diameter of the Airy disk) for  $\lambda = 0.85 \mu\text{m}$  and  $NA = 0.2$  is about  $2.5 \mu\text{m}$ . In view of the numerical examples given above we may disregard these diffraction effects when using multimode fibers.

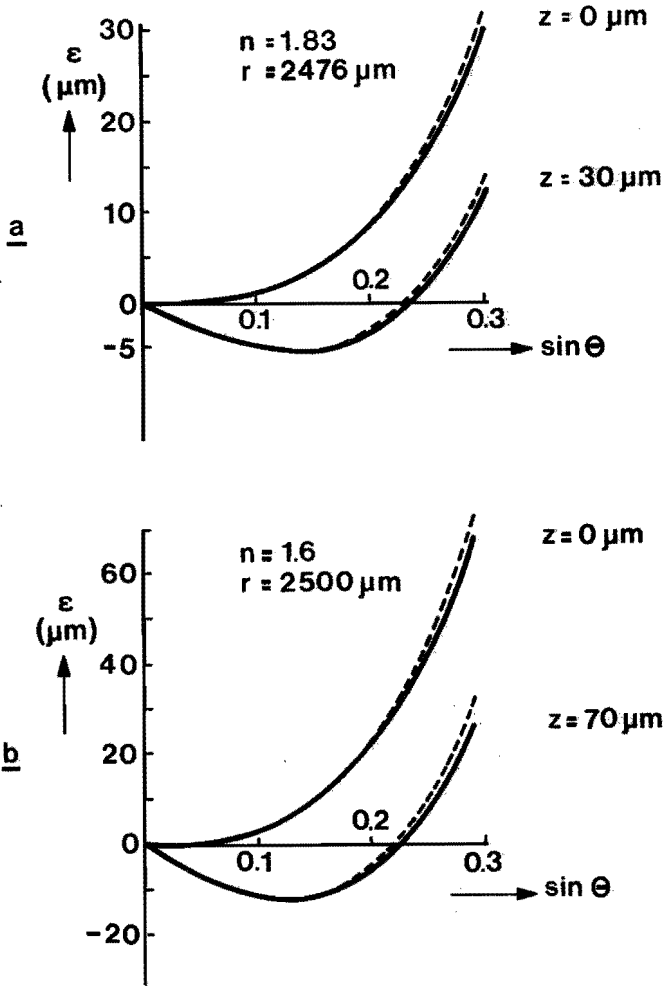


Fig. 1.6 Relationship between transverse spherical aberration  $\epsilon$  and launching angle  $\theta$ , showing the effect of defocused fiber ends. Solid curves were obtained by exact ray-tracing, the dashed ones by third-order aberration theory.

(a) Using high-refractive index ball lenses.

(b) Using low-refractive index ball lenses.

#### 1.4 Coupling Efficiency

It has been estimated by several authors [16–18] that splice losses strongly depend on input power distribution. In all these papers it is pointed out that the uniform distribution causes the highest sensitivity to mismatches in practice. This can also be expected in a lens connection, for as we have seen in Sec. 1.3 the spherical aberration strongly depends on the launching from the input fiber. In this section

we will determine the coupling efficiency of the lens connection described in the previous sections, assuming a uniform distribution in the input fiber. The results will indicate a worst case for practical fiber systems.

The index profile of the fiber is assumed to be [see also Eq.(1.1)]

$$\begin{aligned} n(r) &= n_0 [1 - g^2 a^2 (r/a)^\alpha]^{1/2}, \quad r < a, \\ &= n_0 (1 - g^2 a^2)^{1/2}, \quad r \geq a, \end{aligned} \quad (1.13)$$

where  $a$  is the core radius and  $\alpha$  is a parameter describing the profile:  $\alpha = \infty$  represents a step-index fiber,  $\alpha \cong 2$  a graded-index fiber.

Each point of the emitting fiber end causes a light spot at the receiving fiber end. Due to rotational symmetry only the on-axis point causes a circular light spot. However, the distance between all points and the axis is very small compared with the focal length. Therefore, we assume that the light spot is circular for all points and has the same diameter at equal NA (remember also the remarks concerning the off-axis lens aberrations in Sec. 1.3). We can consider, in good approximation, the coupling problem in the same way as an endface separation in a butt-joint connector (see Fig. 1.7). The only difference is that in the case of separation the diameter of the spot is proportional to  $\theta$ .

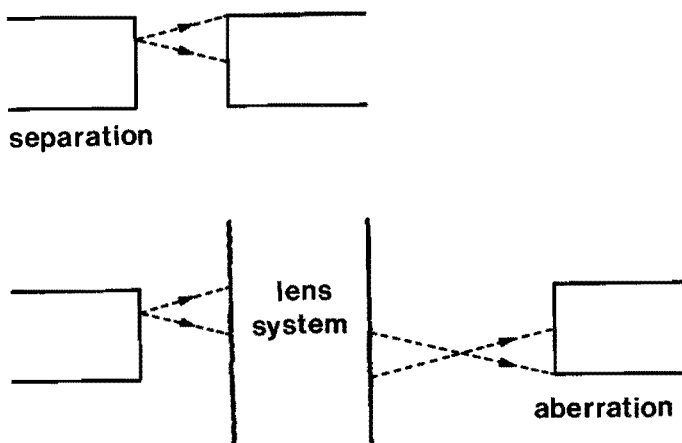


*Fig. 1.7 Correspondence between separation mismatch in butt-joint connections and aberration in a lens coupling*

For the guided power we have (see Fig. 1.8)

$$P = L \int \int \cos\theta \, dA \, d\Omega, \quad (1.14)$$

where  $dA$  is an elemental source with radiance  $L$ , and  $d\Omega$  is an elemental solid angle.

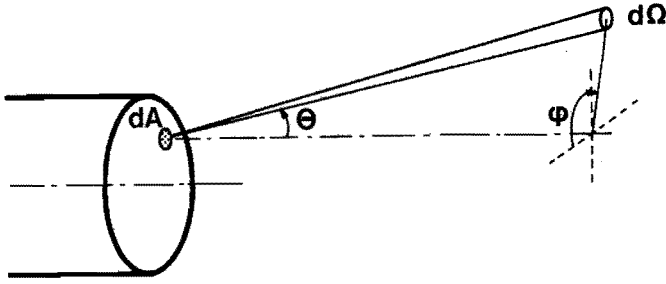


Fig. 1.8 Visualization of ray angles

$L$  is a constant for uniform distributions. For LEDs  $L$  is usually expressed in  $W/Sr/cm^2$ . Next we have to express  $dA$  and  $d\Omega$  in terms of ray angles and coordinates. From Fig. 1.8 we see that

$$d\Omega = \sin\theta \, d\theta \, d\varphi . \quad (1.15)$$

Consider a parallel beam leaving the fiber end at an angle  $\theta$  and having an azimuth  $\varphi$  (see Fig. 1.8). All the rays of this beam originate from a circle with radius  $r_1(\theta)$  at the endface.  $r_1(\theta)$  is the maximum distance from the fiber axis at which rays with angle  $\theta$  are present. Using Eq. (1.13) we get

$$r_1(\theta) = a (1 - \sin^2\theta/NA^2)^{1/\alpha} , \quad (1.16)$$

where

$$NA = n_0 \, ga \quad (1.17)$$

is the on-axis numerical aperture of the fiber.

According to these considerations we can derive for the guided power

$$P = L \int_0^{\theta_c} \int_0^{2\pi} \pi r_1^2(\theta) \sin\theta \cos\theta \, d\theta \, d\varphi , \quad (1.18)$$

where

$$\theta_c = \arcsin(NA) \quad (1.19)$$

is the critical angle.

A straightforward integration of Eq. (1.18) results in the well-know expression for the guided power

$$P = \frac{\alpha}{\alpha + 2} \pi^2 a^2 L NA^2 . \quad (1.20)$$



In the model mentioned before and shown in Fig. 1.7 aberration causes a lateral shift of the circle with radius  $r_1(\theta)$  in the image plane. Considering the lens coupling problem between two identical fibers, we have to replace the term  $\pi r_1^2(\theta)$  in Eq. (1.18) by the overlap  $O$  of two circles with radius  $r_1(\theta)$ , whose centers are at distance  $\epsilon(\theta)$ .

The coupled power  $P$  in this model is obtained from

$$P = 2\pi L NA^2 \int_0^{x_1} O \sin x \cos x \, dx , \quad (1.21)$$

where we have introduced

$$\sin x = \sin\theta / NA . \quad (1.22)$$

Due to rotational symmetry, the integration of  $\varphi$  resulted in a multiplication by  $2\pi$  in Eq. (1.21). Furthermore,  $x_1$  is the value of  $x$  beyond which there is no overlap between the circles.  $x_1$  is obtained by solving the equation

$$|\epsilon(\theta)| = 2r_1(\theta) . \quad (1.23)$$

$\epsilon(\theta)$  is given by Eq. (1.12) or the corresponding relations for the GRIN-rod lens or rod lens.

Using definition (1.22) in Eqs. (1.16) and (1.23) we obtain for Eq. (1.23)

$$C(x_1) = \cos^{2/\alpha} x_1 , \quad (1.24)$$

where

$$C(x) = |\bar{\epsilon}(x)| / 2a . \quad (1.25)$$

$\bar{\epsilon}(x)$  is the counterpart of  $\epsilon(\theta)$  if use is made of the variable  $x$ .

The coupling efficiency  $\eta$  is determined by division of Eqs. (1.21) and (1.20):

$$\eta = \frac{\alpha + 2}{\alpha} \frac{2}{\pi a^2} \int_0^{x_1} O \sin x \cos x \, dx . \quad (1.26)$$

Finally, we insert the explicit expression for the overlap  $O$  in Eq. (1.26), which can be calculated by simple planimetry:

$$\eta = \frac{4}{\pi} \frac{\alpha + 2}{\alpha} \int_0^{x_1} \sin x \cos x \left[ \cos^{4/\alpha} x \arccos(C \cdot \cos^{-2/\alpha} x) - (\cos^{4/\alpha} x - C^2)^{1/2} C \right] dx . \quad (1.27)$$

Assuming  $C(x) \ll 1$  we can approximate Eq. (1.27) by

$$\eta = 1 - \frac{8}{\pi} \frac{\alpha + 2}{\alpha} \int_0^{\pi/2} \sin x \cos^{1+2/\alpha} x C dx . \quad (1.28)$$

At this stage we have to specify  $C(x)$ . We can write it in the form

$$C(x) = | -\Delta_s \sin x + \Delta_a \sin^3 x | . \quad (1.29)$$

This can be seen from Eqs. (1.12) and (1.22).  $\Delta_a$  is the maximum blur circle radius at the receiving fiber end relative to the core diameter in the case of spherical aberration with focused endfaces.  $\Delta_a$  is obtained by division of Eqs. (1.9), (1.10) or (1.11), as the case may be, and the fiber core diameter.  $\Delta_s$  is the maximum spot-radius at the receiving fiber end relative to the core diameter in the case of separation  $2z$ . We have

- (1)  $\Delta_s = (z / a.n_0) NA$  for GRIN-rod lenses,
- (2)  $\Delta_s = (z / a) NA$  for ball lenses,
- (3)  $\Delta_s = (z / a.n) NA$  for rod lenses.

Inserting Eq. (1.29) in (1.28) we finally get

$$\eta = 1 - \frac{8}{\pi} \frac{\alpha + 2}{\alpha} \int_0^{\pi/2} \sin x \cos^{1+2/\alpha} x | -\Delta_s \sin x + \Delta_a \sin^3 x | dx . \quad (1.30)$$

The integration in Eq. (1.30) cannot be carried out analytically for arbitrary values of  $\alpha$ . Fortunately it is possible for the two most interesting cases, i.e. step index:  $\alpha = \infty$  and graded index:  $\alpha = 2$ .

### A. Step index-profile

For step index Eq. (1.30) tends to

$$\eta_{si} = 1 - \frac{8}{\pi} \int_0^{\pi/2} \sin x \cos x | -\Delta_s \sin x + \Delta_a \sin^3 x | dx . \quad (1.31)$$

A straightforward integration gives

$$\eta_{si} = 1 - \frac{8}{\pi} \left[ \frac{1}{5} - \frac{1}{3} \frac{\Delta_s}{\Delta_a} + \frac{4}{15} \left( \frac{\Delta_s}{\Delta_a} \right)^{5/2} \right] \Delta_a . \quad (1.32)$$

The coupling efficiency is optimal if the term between brackets in Eq. (1.32) is minimal. This is obtained for  $\Delta_s/\Delta_a = 2^{-2/3}$ . In that case we find

$$\eta_{si} = 1 - 0.19\Delta_a, \quad (1.33a)$$

$$\Delta_s = 0.63 \Delta_a. \quad (1.33b)$$

### B. Graded index-profile

For graded index we get [see Eq. (1.30)]

$$\eta_{gi} = 1 - \frac{16}{\pi} \int_0^{\pi/2} \sin x \cos^2 x |-\Delta_s \sin x + \Delta_a \sin^3 x| dx. \quad (1.34)$$

A straightforward integration gives

$$\eta_{gi} = 1 - \frac{16}{\pi} \left[ \frac{\pi}{32} - \frac{x_0}{8} - \left( \frac{\pi}{16} - \frac{x_0}{4} \right) \sin^2 x_0 + \left( \frac{1}{8} \sin x_0 - \frac{1}{6} \sin^3 x_0 + \frac{1}{6} \sin^5 x_0 \right) \cos x_0 \right] \Delta_a, \quad (1.35)$$

where  $\sin^2 x_0 = \Delta_s/\Delta_a$ .

The coupling efficiency is optimal if the term between brackets in Eq. (1.35) is minimal. This minimum is reached for  $x_0 \cong 0.79$ .

In that case we get

$$\eta_{gi} = 1 - 0.21\Delta_a, \quad (1.36a)$$

$$\Delta_s = 0.5\Delta_a. \quad (1.36b)$$

Equations (1.33) and (1.36) are powerful tools in designing lens couplings for fibers. For a specified lens and fiber the value  $\Delta_a$  is found from Fig. 1.5. Next  $\eta$  is calculated with Eq. (1.33a) or (1.36a). Finally the defocusing is determined from Eq. (1.33b) or (1.36b). In the case of GRIN-rod lenses and rod lenses, the lens thickness should be smaller by values obtained from Eq. (1.33b) or (1.36b) than the paraxial lens design. We will illustrate the procedure with a numerical example. For a typical graded-index fiber with  $NA = 0.2$ ,  $a = 25 \mu\text{m}$  and a GRIN-rod lens with  $f = 3 \text{ mm}$ ,  $n_0 = 1.55$  we have

$$\epsilon = 0.65 \times 3000 \times (0.2)^3 = 15.6 \mu\text{m} \text{ (see Fig. 1.5),}$$

$$\Delta_a = \epsilon / 2a = 0.312,$$

$$\eta_{gi} = 1 - 0.21 \times 0.312 = 0.934,$$

$$\Delta_s = 0.5 \times 0.312 = 0.156,$$

$$z = (25 \times 1.55 / 0.2) \times 0.156 = 30 \mu\text{m}.$$

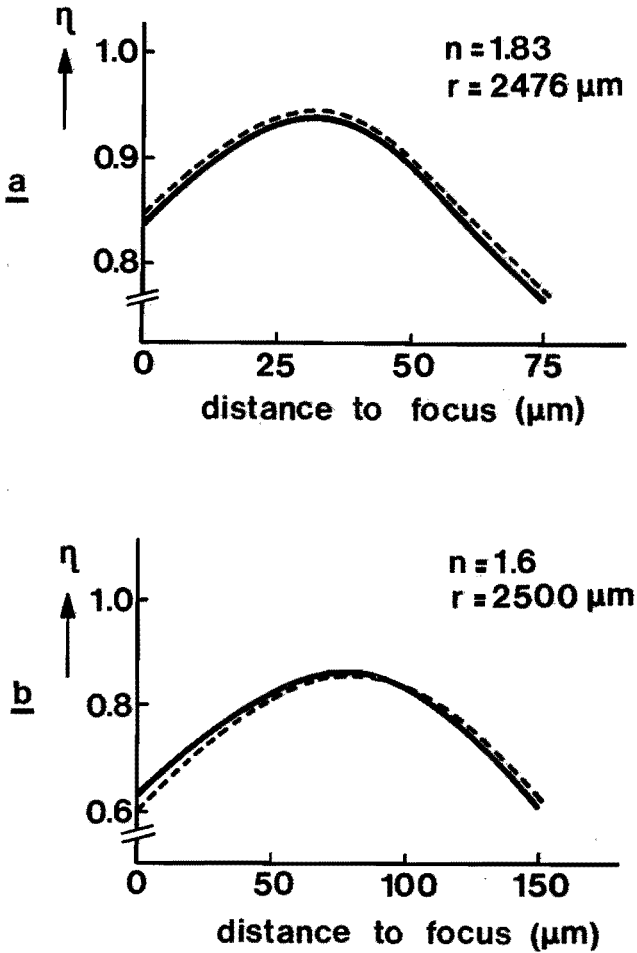


Fig. 1.9 Relationship between coupling efficiency  $\eta$  and defocusing of the fiber ends, for a step-index fiber with a core diameter of  $100 \mu\text{m}$  and  $NA = 0.3$ . Solid curves were obtained by exact ray-tracing, the dashed ones by using the approximations derived in Sec. 1.4.  
 (a) Using high-refractive index ball lenses.  
 (b) Using low-refractive index ball lenses.

In this case, then, the GRIN-rod lens should have a length of a quarter-pitch minus  $30 \mu\text{m}$ .

Note that Eqs. (1.32) and (1.35) are only valid if  $0 \leq \Delta_s/\Delta_a \leq 1$ .

Outside this region one finds in a similar way

$$\eta_{si} = 1 - \frac{8}{\pi} |\Delta_s/3 - \Delta_a/5|, \quad (1.37)$$

$$\eta_{gi} = 1 - |\Delta_s - \Delta_a/2|, \quad \Delta_s/\Delta_a > 1, \Delta_s/\Delta_a < 0, \quad (1.38)$$

where positions larger than the focal length should be expressed by negative values of  $z$ .

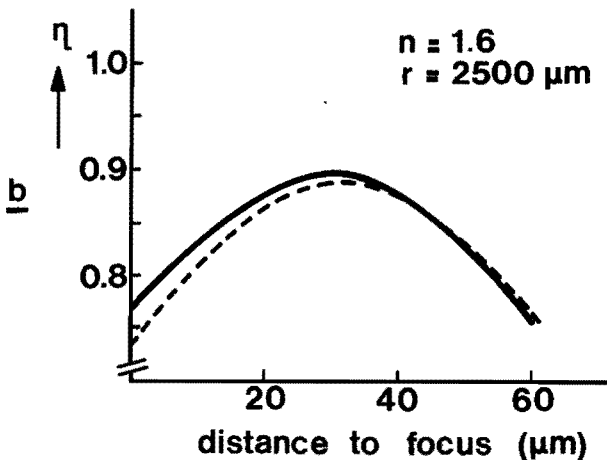
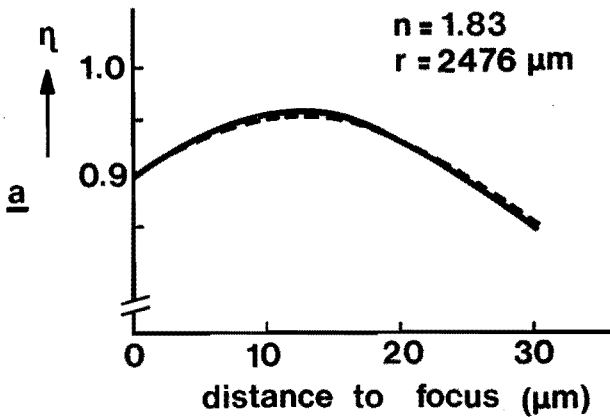


Fig. 1.10 Relationship between coupling efficiency  $\eta$  and defocusing of the fiber ends, for a graded-index fiber with a core diameter of  $50 \mu\text{m}$  and  $NA = 0.21$ . Solid curves were obtained by exact ray-tracing, the dashed ones by using the approximations derived in Sec. 1.4.  
 (a) Using high-refractive index ball lenses.  
 (b) Using low-refractive index ball lenses.

In Figs. 1.9 and 1.10 the coupling efficiency is shown as a function of defocusing. The solid curves were obtained with a computer program using exact ray-tracing techniques and are accurate to within 0.2%. The dashed curves were obtained with the aid of the approximations derived in this section. We see that the approximations lead to results that are in good agreement with the exact values.

If a lens connection is used for a wide range of wavelengths, the focal length of the lens will vary due to the dispersion of the glass. This means that when the wavelength is changed the fiber end will be defocused. Knowing the dispersion, one can calculate the actual focal length and compare it with the one at the wavelength at which the alignment has taken place. The defocusing is then known, and the decrease in coupling efficiency can be calculated with Eqs. (1.32) or (1.35).

### 1.5 Sensitivity to Mismatches

Tolerances of the adjustment of the fiber ends are the same as in butt-joint connections, due to the fact that a 1-1 image is made by the lens system. Relations for these tolerances are well known in literature [16 – 19]. Another problem is the mismatch between two lens-fiber assemblies. In the following we will investigate the lens coupling in the case of three basic mismatches, i.e. separation, offset and tilt.

Assume that the fiber ends in both assemblies emit light, and that this light is projected upon an imaginary screen in the back focal plane. We now consider this projection as a fiber endface. (In Fig. 1.11, this is shown in the case of an offset.) This imaginary fiber has a core radius  $\bar{a}$  :

$$\bar{a} = f NA , \quad (1.39)$$

and a numerical aperture  $\overline{NA}$  :

$$\overline{NA} = a / f . \quad (1.40)$$

We will now use the first-order approximations given by di Vita et al. [19] for the coupling efficiency between two fiber ends in the case of a fiber with core radius  $\bar{a}$  and numerical aperture  $\overline{NA}$ .

If there are no mismatches, the coupling efficiency is limited by spherical aberration. We thus have to multiply the above-mentioned approximations by  $\eta_{\text{opt}}$ .

The resulting formulas are:

Offset d:

$$\eta_{\text{si}} = \eta_{\text{opt}} [1 - 0.64 d / (f.NA)] , \quad (1.41a)$$

$$\eta_{\text{gi}} = \eta_{\text{opt}} [1 - 0.85 d / (f.NA)] . \quad (1.41b)$$

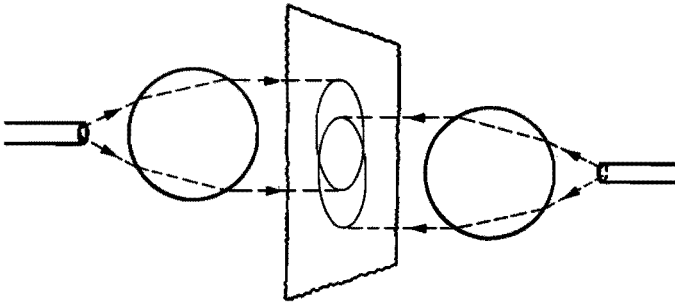


*Fig. 1.11 Visualization of the model used for deriving approximated relations between coupling efficiency and mismatch in lens connections*

Tilt  $\delta$  :

$$\eta_{si} = \eta_{opt} (1 - 0.64 \delta f / a) , \quad (1.42a)$$

$$\eta_{gi} = \eta_{opt} (1 - 0.85 \delta f / a) . \quad (1.42b)$$

Separation  $s$  :

$$\eta_{si} = \eta_{opt} [1 - 0.43 s a / (f^2 NA)] , \quad (1.43a)$$

$$\eta_{gi} = \eta_{opt} [1 - 0.5 s a / (f^2 NA)] . \quad (1.43b)$$

The most critical point in the construction of butt-joint connectors is the transverse alignment [20]. From Eq. (1.41) we see that for a specified fiber this alignment is easier if the focal length is large. Though separation is not a problem in a lens connector, for some fiber-optical devices separations up to 25 mm are needed. This also requires a large focal length. If angular-dispersive devices are used, then the linear dispersion (see chapter 2) is proportional to  $f$ . For a high wavelength selectivity  $f$  should again be large. On the other hand to make  $\eta_{opt}$  as high as possible  $f$  should be chosen small. Thus, it is always necessary to compromise in order to reconcile these contradictory requirements. In Fig. 1.12 a comparison has been made between approximations (1.41) – (1.43) (dashed curves) and exact results. From this we see that for very small mismatches the behavior of the approximated curves differs from that of the exact ones, but outside this region their slopes are the same. This is typically the effect of mismatches between unequal fibers. In our case this means that the image is slightly larger than the receiving fiber, owing to aberrations. In Eqs. (1.41) – (1.43) this effect was neglected. For practical purposes, however, the approximations give a satisfactory indication for tolerances.



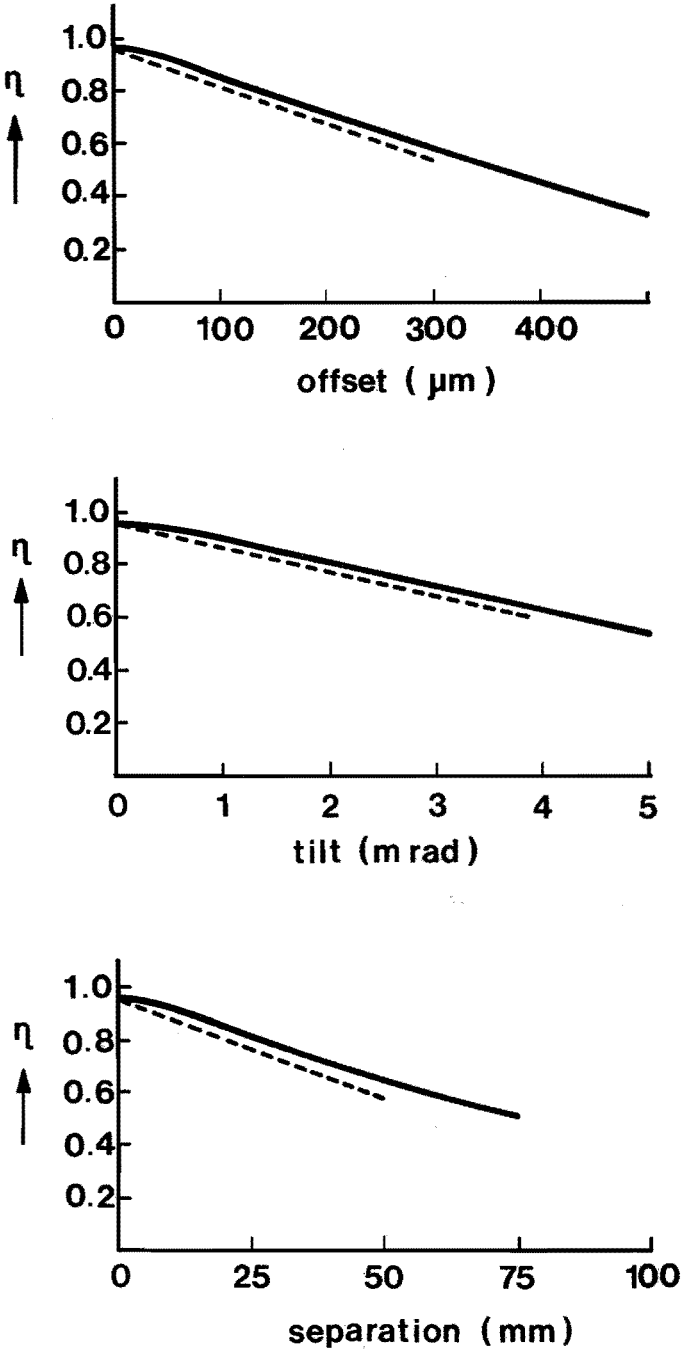
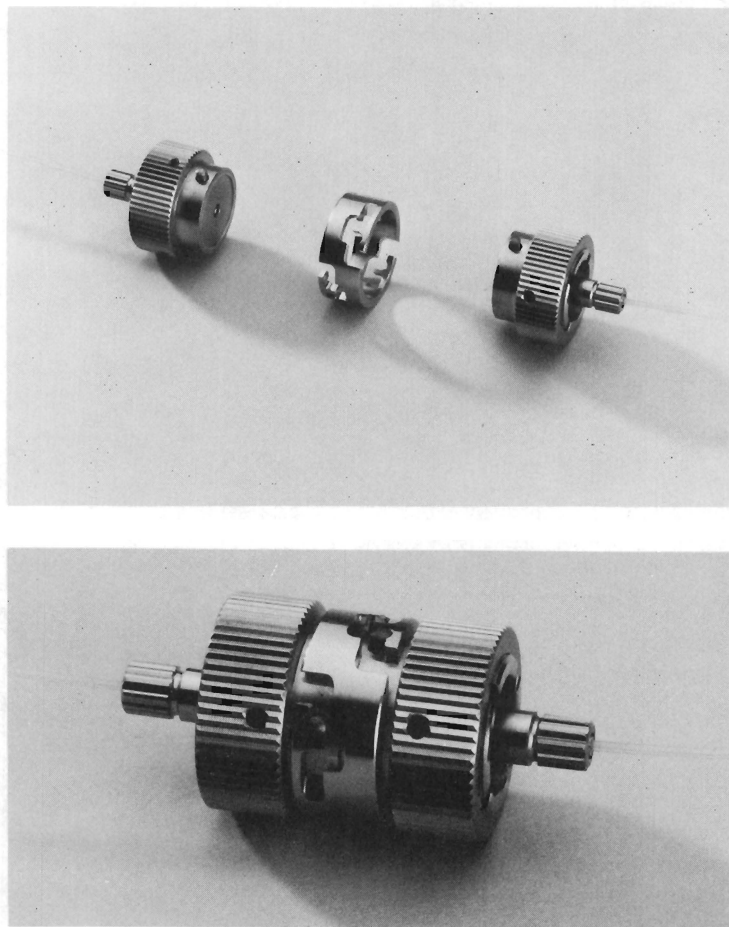


Fig. 1.12 Relationship between coupling efficiency and basic mismatches if ball lenses with  $R = 2476 \mu\text{m}$ ,  $n = 1.83$  and graded-index fibers with a core diameter of  $50 \mu\text{m}$ ,  $NA = 0.21$  are incorporated. Solid curves were obtained by exact ray-tracing techniques, the dashed ones by using the approximations derived in Sec. 1.5.

## 1.6 Experimental Results

In previous sections we have seen that the attainable coupling efficiency of lens connections is nearly the same for the GRIN-rod lens, ball lens and rod lens. The lens type chosen for an actual device will depend on mechanical requirements and optical configuration. For a lens connector we believe that ball lenses are very attractive because they have no orientation dependence and their shape is uncomplicated. These advantages allowed us to design a lens connector that does not contain any precision parts. An initial construction was published some time ago [5]. The present one can be seen in Fig. 1.13. Extended and cutaway views are shown in Fig. 1.14. The principle of alignment is not changed. With the apparatus



*Fig. 1.13 Photographs of the lens connector.*

*(a) Separated.*

*(b) Connected.*

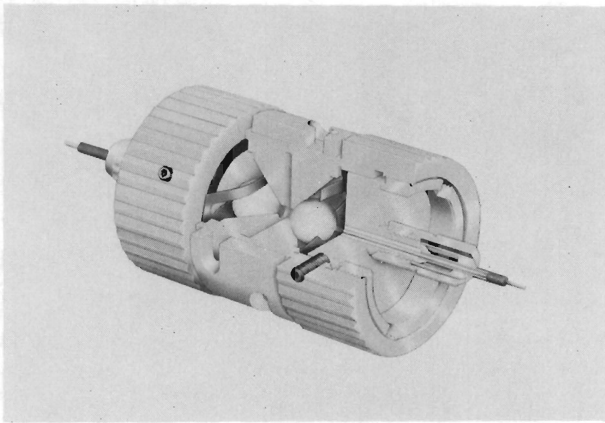
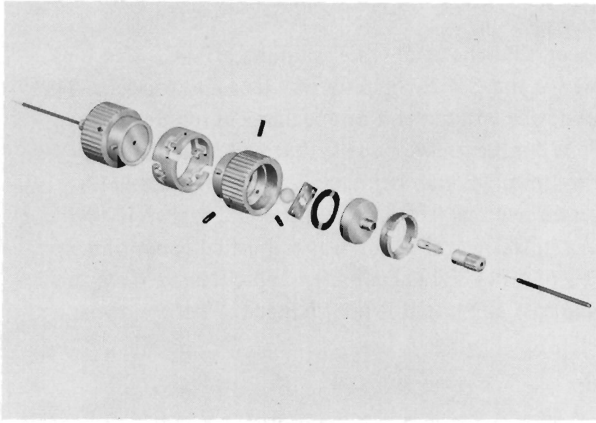


*Fig. 1.14 (a) Extended view of the lens connector,  
(b) Cutaway view of the lens connector.*

based on this principle of alignment the complete procedure takes about five minutes.

The present connector was made in a factory-type of production line and equipped with ball lenses that have  $n = 1.83$  and  $R = 2476 \mu\text{m}$ . Fig. 1.15 shows the statistical results of measured efficiencies of 70 connectors incorporating step-index fibers with a  $100 \mu\text{m}$  core diam and numerical aperture of 0.3. All surfaces were anti-reflection coated and use was made of a LED ( $\lambda_0 = 835 \text{ nm}$ ) for the measurements. The results are seen to be in good agreement with the theoretically predicted efficiency. In Fig. 1.16 a histogram of 68 measured efficiencies is shown.

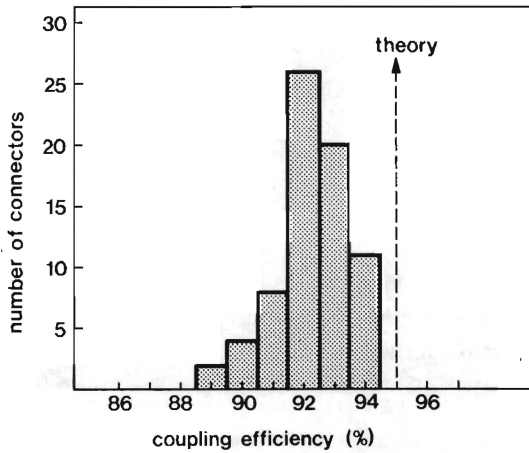


Fig. 1.15 Coupling efficiency of 70 lens connectors, using ball lenses with  $R = 2476 \mu\text{m}$  and  $n = 1.83$ , and incorporating step-index fibers with core diameter of  $100 \mu\text{m}$ ,  $NA = 0.3$ .

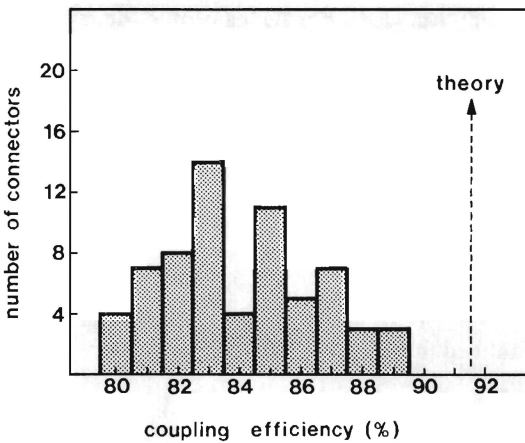


Fig. 1.16 Coupling efficiency of 68 lens connectors, using ball lenses with  $R = 2476 \mu\text{m}$  and  $n = 1.83$ , and incorporating graded-index fibers with core diameter of  $50 \mu\text{m}$ ,  $NA = 0.26$ .

These lens connectors incorporate graded-index fibers with a  $50 \mu\text{m}$  core diam and a numerical aperture of 0.26. The most remarkable difference between Figs. 1.15 and 1.16 is the deviation. When the fiber end is imaged on a screen a sharp core-cladding boundary is seen in the case of a step-index fiber, whereas with a graded-index fiber this boundary is imaged very unclearly. In the latter case, then, the focal alignment is less accurate, which causes a larger deviation in the coupling efficiencies. Here again it should be noted that the LED excitation gives the worst case results in practice. Measurements with steady-state excitation by means of a mode

scrambler showed that the mean value of the coupling efficiencies increased to 90% if graded-index fibers were incorporated (compare with Fig. 1.16).

We also performed some bench experiments with GRIN-rod lenses. These had  $g = 0.3 \text{ mm}^{-1}$ ,  $n_0 = 1.616$  and  $f = 2.06 \text{ mm}$ . The length was a quarter-pitch, so proper defocusing was not possible:  $\Delta_s = 0$ , and for this case Eq. (1.35) reduces to

$$\eta_{gi} = 1 - 0.5 \Delta_a . \quad (1.44)$$

From Fig. 1.5 we see that these parameters yield  $\Delta_a = 0.45$  ( $a = 25 \text{ }\mu\text{m}$ ,  $\text{NA} = 0.26$ ), giving a coupling efficiency with a value of 77.5%. The measurements resulted in a value of 80%, which is very close to the theoretical value.

Note that the efficiency could be improved to 90% if the length of the lenses was decreased by  $35 \text{ }\mu\text{m}$ .

## APPENDIX A

In this Appendix we investigate the spherical aberration of a half-pitch GRIN-rod lens with a parabolic distribution given by Eq. (1.8). For such a profile the ray trajectories are described by [7]

$$M_0^2 \frac{d^2 r}{dz^2} + n_0^2 g^2 r = 0 , \quad (A1)$$

where the constant  $M_0$  is given by

$$M_0 = n(r) \cos\theta . \quad (A2)$$

The ray angles and coordinates are defined in Fig. 1.17.

For rays emitted on the optical axis at  $z = 0$ , we have

$$\frac{d^2 r}{dz^2} + \frac{g^2}{\cos^2\theta_0} r = 0 , \quad (A3)$$

where  $\theta_0$  is the launching angle.

The solution of Eq. (A3) is

$$r = \frac{\sin\theta_0}{g} \sin\left(\frac{gz}{\cos\theta_0}\right) . \quad (A4)$$

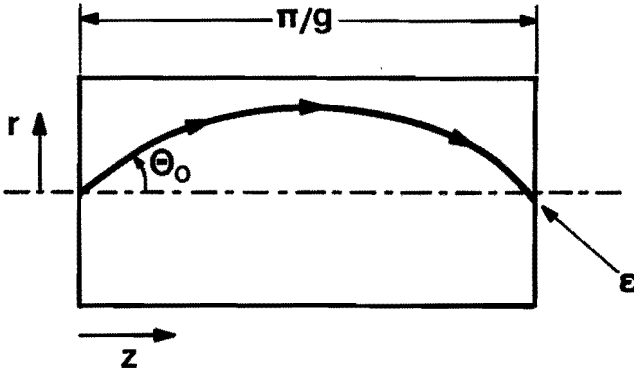


Fig. 1.17 Ray-path in a GRIN-rod lens with a half-pitch length

In the receiving focal plane the distance to the axis (at half-pitch  $z = \pi/g$ ) is

$$\epsilon = \frac{\sin\theta_0}{g} \sin\left(\frac{\pi}{\cos\theta_0}\right). \quad (\text{A5})$$

Third-order approximation of Eq. (A5) gives

$$\epsilon \cong -\frac{1}{2} \frac{\pi}{g} \theta_0^3. \quad (\text{A6})$$

Taking into account the refraction at the front face of the lens, we finally obtain Eq. (1.9).

## APPENDIX B

In this Appendix we investigate the spherical aberration of the ball lens system shown in Fig. 1.18. We first calculate the place B where a ray emitted at focal point E with angle  $\theta$  crosses the optical axis. The sine rule applied in triangle EAO<sub>1</sub> gives

$$\sin\theta_1 = (f/R) \sin\theta, \quad (\text{B1})$$

where  $f$  is the focal length given by Eq. (1.4). After some manipulation we find for the deviation angle  $\delta$  with the optical axis

$$\delta = 2(\theta_1 - \theta_2) - \theta. \quad (\text{B2})$$

Combination of Eqs. (B1) and (B2) and Snells law gives

$$\delta = 2 \left\{ \arcsin \left[ \left( \frac{f}{R} \right) \sin \theta \right] - \arcsin \left[ \left( \frac{f}{nR} \right) \sin \theta \right] \right\} - \theta . \quad (\text{B3})$$

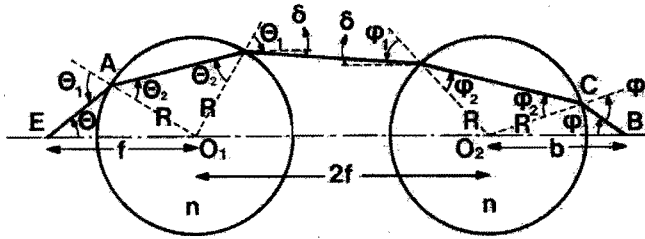


Fig. 1.18 Ray-path in the ball lens system

Taking into account only terms up to third order in  $\theta$ , Eq. (B3) reduces to

$$\delta \cong \frac{1}{8} \left[ \frac{n}{(n-1)^2} - 1 \right] \theta^3 . \quad (\text{B4})$$

For the angle  $\varphi$  a relation similar to Eq. (B2) holds:

$$\varphi = 2(\varphi_1 - \varphi_2) + \delta . \quad (\text{B5})$$

From Fig. 1.18 we see that  $\varphi_1 \cong \theta_1$  because  $\delta \ll \varphi_1, \theta_1$ . Keeping this in mind we can approximate Eq. (B5) by

$$\varphi = \theta + 2\delta . \quad (\text{B6})$$

Application of the sine rule in triangle  $O_2CB$  leads to

$$b = R \frac{\sin \varphi_1}{\sin \varphi} . \quad (\text{B7})$$

Thus for the transversal aberration  $e$  in the focal plane we get

$$e = \left( f - R \frac{\sin \varphi_1}{\sin \varphi} \right) \tan \varphi . \quad (\text{B8})$$



Using Eqs. (B1) and (B6) we can approximate Eq. (B8) by

$$\epsilon = \left[ 1 - \frac{\sin\theta}{\sin(\theta+2\delta)} \right] f \tan(\theta+2\delta), \quad (\text{B9})$$

which can be rewritten to

$$\epsilon \cong 2\delta f. \quad (\text{B10})$$

The combination of Eqs. (B4) and (B10) finally leads to Eq. (1.10).

## REFERENCES

1. K. Thyagarajan, A. Rohra, and A.K. Ghatak, *Appl. Opt.* 19, 266 (1980).
2. W.J. Tomlinson, *Appl. Opt.* 19, 1117 (1980).
3. W.J. Tomlinson, *Appl. Opt.* 16, 2180 (1977).
4. K. Kobayashi et al., *Fiber Integrated Opt.* 2, 1 (1979).
5. A. Nicia, *Electron. Lett.* 14, 511 (1978).
6. J.C. North and J.H. Stewart, *Digest, Fifth ECOC, Amsterdam 1979*, paper 9-4.
7. K. Iga, *Appl. Opt.* 19, 1039 (1980).
8. M. Kawazu and Y. Ogura, *Appl. Opt.* 19, 1105 (1980).
9. F.A. Jenkins and H.E. White, *Fundamentals of Optics* (McGraw-Hill, New York, 1976), pp. 84 – 87.
10. K. Aoyama and J. Minowa, *Appl. Opt.* 18, 2834 (1979).
11. S. Kawakami and J. Nishizawa, *IEEE Trans. Microwave Theory Techn.* 16, 814 (1968).
12. D.T. Moore, *Appl. Opt.* 19, 1035 (1980).
13. A.R. Cooper and M.A. El-Leil, *Appl. Opt.* 19, 1087 (1980).
14. SLS Selfoc Micro Lens, Nippon Sheet Glass Co. Ltd.
15. *Optical Glass Catalog 3050/66*, Schott.
16. C.M. Miller and S.C. Mettler, *Bell Syst. Techn. J.* 57, 3167 (1978).
17. D. Gloge, *Bell Syst. Techn. J.* 55, 905 (1976).
18. Y. Daido, T. Iwama, and E. Miyauchi, *Trans. Inst. Electron. Commun. Eng. Jpn.* 61-E, 816 (1978).
19. P. di Vita and U. Rossi, *Opt. Quantum Electron.* 10, 107 (1978).
20. K. Nawata, *IEEE J. Quantum Electron.* QE-16, 618 (1980).

## 2. GENERAL CONSIDERATIONS FOR WAVELENGTH DIVISION MULTIPLEXING

### 2.1 Introduction

Wavelength Division Multiplexing (WDM) is a technique in which a number of signals, each carrying its own information, are transmitted over a single fiber at different wavelengths [1]. The technique has attracted much attention since the first experimental results were reported in 1977, because WDM will become indispensable for the local network. Recent studies have shown that it is possible to have very elegant fiber-optical subscriber loops with WDM, showing a high degree of integration for telephone, TV, and data services [2]. Another important aspect is the increased transmission capacity of a single fiber. Trunk transmission in the long-wavelength region, where cable costs are dominant, can effectively use WDM for economy.

A general scheme for a WDM system is shown in Fig. 2.1. These systems can operate with one-way or two-way transmission. Many variants are conceivable, but only one-way transmission will be considered here. For most of the feasible WDM systems the considerations have only to be adapted slightly.

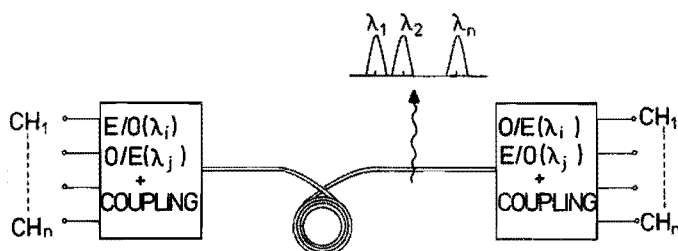


Fig. 2.1 General structure of a WDM system

The functions needed are:

- (a) transmitter side: E/O transduction ( $\lambda_i$ ) plus coupling to transmission fiber,
- (b) receiver side: O/E transduction plus coupling to photodiode, where  $\lambda_i$  is the parameter.

In future these functions should be realized by means of electro-optical integrated circuits. In the present state of the art, however, only two alternatives are available:

- (1) one transducer for all channels,
- (2) one transducer for each channel plus optical (de)multiplexers.

As far as the first alternative is concerned, this aspect of WDM has not attracted much attention, due to the considerable technological problems involved. Monolithically integrated DFB lasers with different grating periods and passive waveguides on a GaAs substrate were reported in Ref. 3. The wavelength separation

obtained was only 2 nm. Some work has also been done on dual-wavelength LEDs and wavelength demultiplexing photodiodes [4 – 6]. At present, however, practical WDM transmission is only possible using the approach mentioned in (2), where all the work has been concentrated on the optical multiplexer and demultiplexer (see Fig. 2.2).

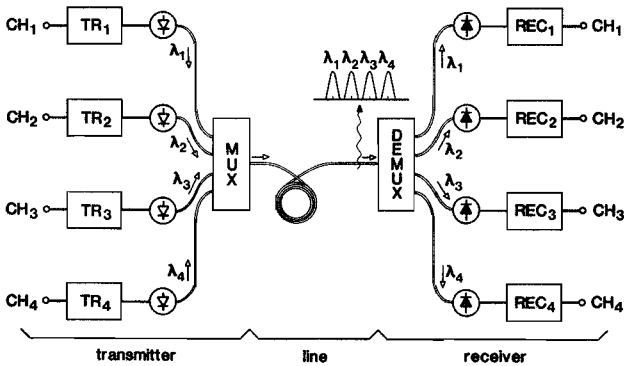


Fig. 2.2 Schematic diagram of a WDM system using optical multiplexers and demultiplexers

## 2.2 Optical Multiplexers

At the transmitter end of a system (see Fig. 2.2), the power distribution in the fiber greatly depends on the launching conditions, and will be different for each laser pigtail. For this reason we assume a uniform distribution, this being the worst case in practice. In the case of wavelength-independent structures, the intensity law of geometrical optics tells us that the fundamental insertion loss of an  $N$ -channel multiplexer is  $10 \log N$  dB if input and output fibers are identical. The minimum loss of, for example, a four-channel multiplexer would be 6 dB, which is unacceptable high. This limitation due to the intensity law can be avoided in two ways, by using:

- (1) wavelength-selective components,
- (2) input fibers, that are undersized as regards the core and/or numerical aperture.

An overview of wavelength-selective devices, mainly intended for demultiplexing, is given in section 2.3. Although such devices can also be used for multiplexing, other structures are often preferable because a multiplexer has no wavelength-discriminating function. This will be explained in the following. Without going into detail now (details are given in section 2.3), it is noted that wavelength-selective multiplexers are hampered by the following disadvantages:

- (a) High lens-coupling losses can hardly be avoided if the input fibers and the output fiber are all identical.

- (b) Wavelength-selective components cause additional loss (Peak transmission of interference filters is  $\sim 85\%$  maximum, grating efficiency is limited to  $\sim 80\%$ ).
- (c) The last source of insertion loss we mention is the spectral behavior of such multiplexers. Any deviation from the desired laser peak wavelength will increase the loss, because it is not possible to have a flat pass band as it is in a demultiplexer, where large step-index output fibers are used.

The losses mentioned under (a) and (c) are eliminated or reduced if undersized input fibers are used. The above-mentioned considerations indicate that every multiplexer has to contain undersized input fibers. However, when such fibers are used it is possible for one-way transmission to design low-loss multiplexers without wavelength-selective components, as will be discussed in the chapter dealing with the design of optical multiplexers. It will be clear that such multiplexers have the advantage of being independent of the operating wavelength.

In the following we derive some fundamental limits for insertion loss in wavelength-independent multiplexers.

Assuming a uniform distribution, one can easily derive for the guided power  $P$  in a graded-index fiber with a parabolic index-profile

$$P = \frac{\pi^2}{2} a^2 L NA^2 , \quad (2.1)$$

where  $a$  is the core radius,  $NA$  is the on-axis numerical aperture, and  $L$  is the radiance, which is assumed to be a constant. For LEDs  $L$  is usually expressed in  $W/Str/cm^2$ . At any point of a passive optical system the spectrum of  $L$  cannot exceed the spectrum of  $L$  at the input. Keeping in mind this fundamental law, we apply Eq. (2.1) to wavelength-independent multiplexers. For the total input power  $P_i$  of an  $N$ -channel multiplexer we have

$$P_i = (N/2)\pi^2 a_1^2 L NA_1^2 , \quad (2.2)$$

where  $a_1$  is the core radius and  $NA_1$  is the on-axis numerical aperture of the input fibers. A lower bound for the insertion loss  $I$  of the multiplexer under uniform launching conditions can be obtained by division of Eq. (2.1), applied to the output fiber, and Eq. (2.2):

$$I = 10 \log N - 20 \log \left( \frac{a_0 NA_0}{a_1 NA_1} \right) \text{ dB} , \quad (2.3)$$

where  $a_0$  and  $NA_0$  are the parameters of the output fiber. Eq. (2.3) concerns the loss of each channel if the structure, seen from each input fiber, is the same. Loss-free operation is only possible if

$$N^{1/2} a_1 NA_1 \leq a_0 NA_0 . \quad (2.4)$$

In practice the requirement for loss-free operation will be stricter than condition (2.4), because of the circularity of fibers and lenses.

### 2.3 Optical Demultiplexers

Demultiplexers, of course, have a wavelength-discriminating function. Because light rays are characterized by: (1) direction, (2) intensity, and (3) wavelength, it is necessary to insert between input and output fibers wavelength-selective components, a principle of operation which is based on dispersion of the refractive index (bulk property), or on interference effects. These components change the direction and/or intensity of the incident light with the wavelength as the parameter. As all these components are sensitive to the direction of the incident light the divergent light radiated from the fiber end is collimated before impinging upon the dispersive element, and decollimated after leaving it. In Table 2.1 a classification is made according to the principle of operation. The corresponding elements are listed at the cross-points of the matrix. In the following each of these principles will be reviewed briefly.

Based on Operates on	Material Properties	Interference Effects
Direction	Prism	Grating
Intensity	Junction Glass - 1 Glass - 2	Thin Film Filter

Table 2.1 Classification of wavelength selection according to the principle of operation

All angular-dispersive devices can be represented schematically as shown in Fig. 2.3.

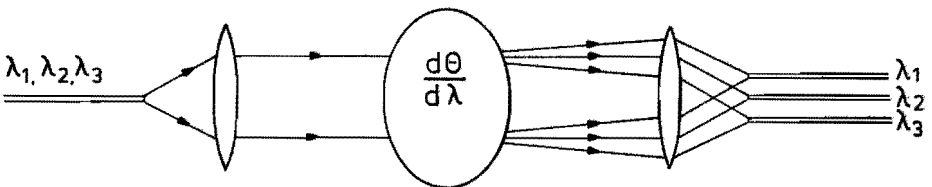


Fig. 2.3 Schematic drawing of a demultiplexer using an angular-dispersive element

The signal from the input fiber is collimated, passed through the dispersive element, and the resulting beams are then focused on the output fibers. The linear dispersion at the position of the output fibers is

$$\frac{dx}{d\lambda} = f \frac{d\theta}{d\lambda}, \quad (2.5)$$

where  $f$  is the focal length of the focusing optics and  $d\theta/d\lambda$  is the angular dispersion of the dispersive element. For angular-dispersive devices the outputs (or inputs in the case of a multiplexer) are located physically close together. Their precise spacing is an important parameter, because it affects the insertion loss and cross-talk of the pass bands.

*Prism:* Typical schematic designs for prism demultiplexers are shown in Fig. 2.4.

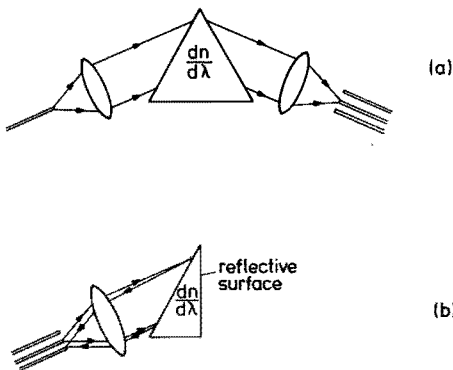


Fig. 2.4 Demultiplexers using a dispersive prism.

(a) Transmission mode

(b) Reflection (Littrow) mode

The two designs are nearly equivalent optically, but the Littrow configuration (Fig. 2.4b) is most attractive because it requires only one lens. For a prism the angular dispersion is given by

$$\frac{d\theta}{d\lambda} = \frac{d\theta}{dn} \frac{dn}{d\lambda}, \quad (2.6)$$

where the first factor depends on the geometry of the configuration, and the second factor is an intrinsic property of the material. To minimize astigmatism it is necessary to operate close to the minimum deviation angle, and in this case  $d\theta/d\lambda$  is given by

$$\frac{d\theta}{d\lambda} = \frac{\tan(\delta/2)}{[1 - n^2 \sin^2(\delta/2)]^{1/2}} \frac{dn}{d\lambda}, \quad (2.7)$$

where  $\delta$  is the refracting angle of the prism (according to the configuration shown in Fig. 2.4a). With highly dispersive materials, dispersion up to  $d\theta/d\lambda \cong 2.10^{-4}$  rad/nm can be obtained ( $\delta = 45^\circ$ ).

**Grating:** A blazed or holographic reflection grating is the best choice with respect to the diffraction efficiency. For demultiplexers using a reflection grating as the wavelength-sensitive device it is probably most convenient to use the Littrow mounting, as illustrated in Fig. 2.5.

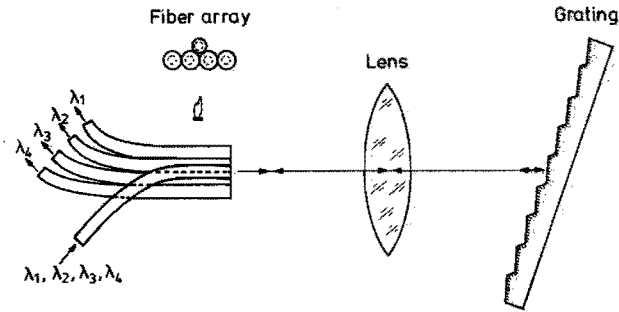


Fig. 2.5 Demultiplexer using a blazed plane reflection grating

This mounting minimizes astigmatism and utilizes the same optics for input and output [1]. The angular properties of a grating in a first order Littrow mounting are described by

$$\frac{d\theta}{d\lambda} = \frac{1}{(\Lambda^2 - \lambda^2/4)^{1/2}}, \quad (2.8)$$

where  $\Lambda$  is the grating period, and  $\lambda$  is the operating wavelength. For commonly used 1200 grooves/mm gratings one can obtain  $d\theta/d\lambda \cong 10^{-3}$  rad/nm, which is one order of magnitude higher than the maximum values occurring with prisms.

**Glass1-glass2 junction** [7]: This principle of operation is illustrated schematically in Fig. 2.6. Wavelength selection is achieved by a junction of two types of glasses whose refractive indices satisfy two conditions, viz.

$$n_1(\lambda_1) = n_2(\lambda_1), \quad (2.9)$$

and

$$n_1(\lambda_2) < n_2(\lambda_2). \quad (2.10)$$



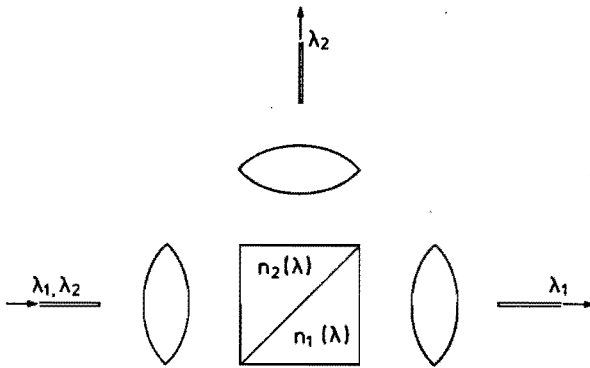


*Fig. 2.6 Wavelength selection by a boundary between two different glasses*

Thus, at  $\lambda_1$  the light does not see the junction and is coupled to fiber 1. For the other wavelength,  $\lambda_2$ , condition (2.10) is such that the light is totally reflected at the junction and coupled to fiber 2. Owing to the absence of suitable materials, no practical devices have so far been constructed.

**Interference filter:** Such filters usually consist of a stack of thin dielectric layers, with alternating high and low refractive index, which are evaporated onto a transparent substrate. Filter designs of up to 40 layers are technologically possible, and use is currently being made of  $\lambda/4$  and  $\lambda/2$  optical layer thicknesses. The available dielectric materials show no absorption, so the reflection curve plus transmission curve is everywhere 100%. For the sake of illustration one of the many possible structures is shown in Fig. 2.7.

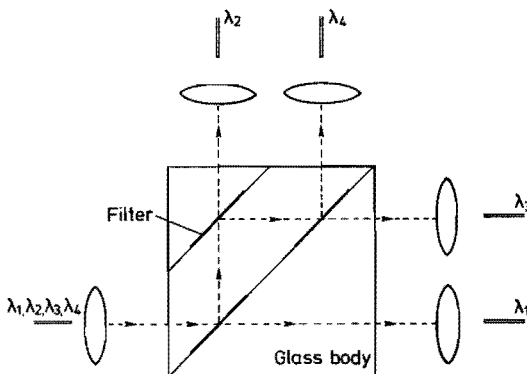


*Fig. 2.7 Demultiplexer structure using dichroic beam splitters*

## 2.4 External Conditions for Multi/Demultiplexers

In section 2.2 it was pointed out that with decreasing values of the input fiber parameters a higher attainable multiplexer efficiency will be found. In addition, the influence of these smaller values of the fiber parameters on the coupling efficiency with the light source should also be considered. Another aspect in micro-optical multi/demultiplexers is the lens coupling between unequal input and output fibers. For a better understanding of the behavior of multi/demultiplexers it is necessary to study the influence of lens aberrations in these devices.

### 2.4.1 Laser-Fiber Coupling

At this stage we will investigate how the fiber parameters affect the laser coupling.

#### A. Field Distributions of Laser and Fiber

In the TEM approximation all field components satisfy the scalar wave equation. Both in free space and in a medium with a radial parabolic-index distribution, separation of the variables is possible. For this reason we have only to consider 2-D beams and modes in the plane either perpendicular or parallel to the junction plane of the laser diode. The total field is then obtained by multiplication of these 2-D field expressions.

The radiated light in laser diodes in normal operation is satisfactorily described by a fundamental Gaussian beam [8, 9]. However, the nature of this beam is rather complex. The field pattern of the laser is characterized by three geometrical parameters (and in addition by the emitting wavelength  $\lambda_0$ ). Most commonly used are: (1)  $\theta_{\perp}$  = full width at half maximum (FWHM) of intensity of the far field perpendicular to the junction plane (see Fig. 2.8), (2)  $\theta_{\parallel}$  = FWHM of intensity of the far field parallel to the junction plane, (3)  $\Delta$  = astigmatism, that is, when gain-guiding predominates in the junction plane, the beam waist parallel to the junction is virtual, and it is displaced by a virtual distance  $\Delta$  behind the laser facet. At the same time, the waist perpendicular to the junction plane remains at the laser facet due to index-guiding in this plane. In other words, the astigmatism  $\Delta$  is defined as the virtual distance between the beam waists in both planes having a width of  $2\omega_{\perp}$  and  $2\omega_{\parallel}$  (virtual) (see also Fig. 2.9).

In Cartesian coordinates the transverse field distribution of the 2-D fundamental Gaussian beam in free space is described by [10]

$$\psi_1(x) = \left( \sqrt{\frac{2}{\pi}} \frac{1}{\omega_z} \right)^{1/2} \exp \left( -\frac{x^2}{\omega_z^2} + ik_0 \frac{x^2}{2R} \right), \quad (2.11)$$

where the beam width  $2\omega_z$  at a distance  $z$  from the beam waist (Fig. 2.10) is

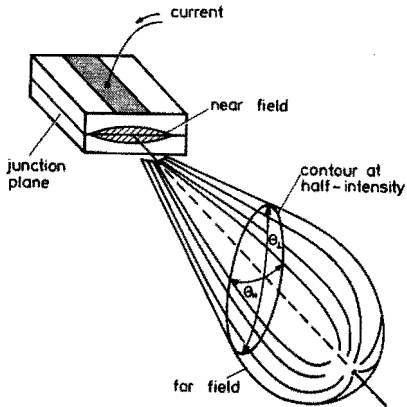


Fig. 2.8 Radiation pattern of a laser diode.  $\theta_{\perp}$  and  $\theta_{\parallel}$  are FWHM of intensity of the far-field, perpendicular and parallel to the junction plane, respectively

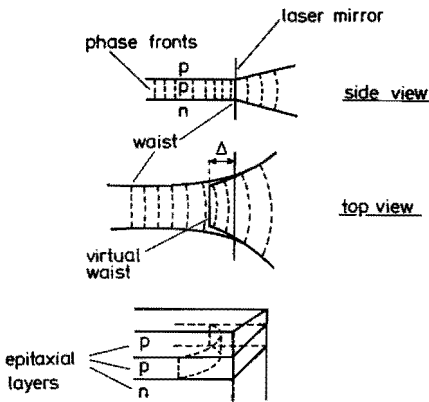


Fig. 2.9 Phase fronts of an astigmatic laser diode

$$\omega_z = \omega_i \left[ 1 + \left( \frac{2z}{k_0 \omega_i^2} \right)^2 \right]^{1/2}, \quad (2.12)$$

and the wave front curvature  $R$  is

$$R = z \left[ 1 + \left( \frac{k_0 \omega_i^2}{2z} \right)^2 \right]. \quad (2.13)$$

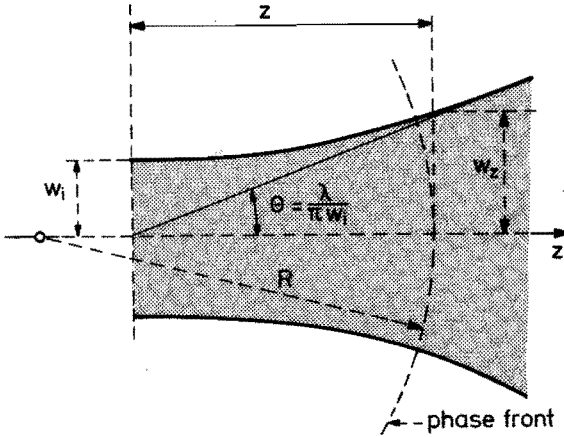


Fig. 2.10 Contour of a Gaussian beam

Here  $2\omega_1$  is the beam width at the waist ( $z = 0$ ), and  $k_0 = 2\pi/\lambda_0$  is the free-space wave number. The  $z$ -axis is chosen along the direction of propagation of the beam but has different origins for the  $\perp$  and  $\parallel$  planes. Furthermore the field amplitude has been normalized:

$$\int_{-\infty}^{\infty} |\psi_1(x)|^2 dx = 1 \quad (2.14)$$

It is assumed that the fiber has a parabolic refractive index distribution. As far as the launching efficiency is concerned a nonparabolic index does not significantly alter the following results and conclusions if the deviation from a parabolic index-profile is small.

Consider an infinite-parabolic medium, whose refractive index is given by

$$n(r) = n_0 (1 - g^2 r^2)^{1/2}, \quad (2.15)$$

where  $n_0$  is the on-axis index, and  $g$  is a constant.

Bounded modes in an infinite-parabolic medium, after separation of the variables in the scalar wave equation, are expressed as [11] (in one transverse direction)

$$\psi_m(x) = \left( \sqrt{\frac{2}{\pi}} \frac{1}{2^{m/2} m! \omega_0} \right)^{1/2} H_m(x\sqrt{2}/\omega_0) \exp(-x^2/\omega_0^2), \quad (2.16)$$

where  $H_m(x)$  is the Hermite polynomial of order  $m$ , one of the transverse mode numbers, and  $\omega_0$  is the characteristic spot size of the fiber defined by

$$\omega_0^2 = \lambda_0 / (\pi n_0 g) \quad (2.17)$$

The propagation constants of these modes are

$$\beta_{mn}^2 = k_0^2 n_0^2 \left[ 1 - \frac{4(m+n+1)}{k_0^2 n_0^2 \omega_0^2} \right] , \quad (2.18)$$

where  $m$  and  $n$  are the transverse mode numbers.

The finite core radius of the fiber, however, limits the permissible number of propagation modes. The condition for the modes that are propagating without radiation loss due to the finite core radius is given by [12]

$$k_0^2 n_0^2 (1 - g^2 a^2) - \beta_{mn}^2 < 0 , \quad (2.19)$$

where  $a$  is the core radius.

From Eqs. (2.18) and (2.19) it follows that

$$2(m+n+1) < \frac{2\pi}{\lambda_0} a \text{ NA} . \quad (2.20)$$

NA is the on-axis numerical aperture of the fiber:

$$\text{NA} = n_0 g a . \quad (2.21)$$

Apart from the fundamental Gaussian mode, as in a single-mode fiber, several higher-order Gaussian modes can propagate in the multimode graded-index fiber. For this reason, the beam emerging from the endface can be described by Gaussian beams of an order corresponding to the associated fiber mode and with a waist  $\omega_0$  located at the endface. Condition (2.20) prescribes the permissible orders that correspond to bounded modes of the fiber.

## B. Excitation of the Fiber Modes by a Gaussian Beam

It is assumed that the input beam is launched centrally along the axis of the fiber and that reflections from the fiber endface can be neglected due to a proper anti-reflection coating.

The power transfer from an incoming fundamental Gaussian beam (laser diode) to a set of Gaussian fiber modes is described by coupling and conversion coefficients, which have been evaluated analytically by Kogelnik [13]. In the following we apply some of his results.

To evaluate the coupling coefficients, the field distributions of the laser and fiber are equated in the input plane of the fiber:

$$\psi_{\perp}(x)\psi_{\parallel}(y) = \sum_m \sum_n c_{mn} \psi_m(x) \psi_n(y) . \quad (2.22)$$

(Remember also the remarks concerning the separation of the variables.) Here  $\psi_{\perp}(x) \cdot \psi_{\parallel}(y)$  represents the incoming laser field, of which each term represents a 2-D beam in the plane perpendicular and parallel to the junction plane, respectively, described by Eq. (2.11). Similarly  $\psi_m(x) \cdot \psi_n(y)$  is the fiber mode (m, n) given by Eq. (2.16).  $c_{mn}$  denotes the corresponding excitation coefficient. Invoking the orthonormality of the mode functions given by Eq. (2.16) in Eq. (2.22), one notes that

$$|c_{mn}|^2 = |\alpha_m^{\perp}|^2 \cdot |\alpha_n^{\parallel}|^2, \quad (2.23)$$

which describes the power coupling of the laser field with the fiber mode (m, n).  $|\alpha_m^{\perp}|^2$  and  $|\alpha_n^{\parallel}|^2$  can be calculated from

$$|\alpha_m^{\perp, \parallel}|^2 = \frac{m!}{2^m [(m/2)!]^2} \sqrt{\kappa_{\perp, \parallel}} (1 - \kappa_{\perp, \parallel})^{m/2}, \quad m = \text{even}. \quad (2.24)$$

Due to the axial launching only even fiber modes are excited.  $\kappa_{\perp, \parallel}$  is the fraction of power transferred from a symmetric laser beam with waist  $\omega_{\perp, \parallel}$  at a distance  $z_{\perp, \parallel}$  from the fiber endface into the fundamental mode of the fiber.  $\kappa_{\perp, \parallel}$  is given by

$$\kappa_{\perp, \parallel} = \frac{4W_{\perp, \parallel}^2}{(1 + W_{\perp, \parallel}^2)^2 + [2z_{\perp, \parallel} / (k_0 \omega_0^2)]^2}, \quad (2.25)$$

where

$$W_{\perp, \parallel} = \omega_{\perp, \parallel} / \omega_0. \quad (2.26)$$

Next, the overall launching efficiency  $\eta$  of the fiber is expressed as

$$\eta = \sum_m \sum_n |\alpha_m^{\perp}|^2 \cdot |\alpha_n^{\parallel}|^2, \quad \frac{m}{2} + \frac{n}{2} \leq M, \quad m, n = \text{even}, \quad (2.27)$$

with

$$M = \text{entier} [a \text{ NA } \pi / (2\lambda_0) - 1/2]. \quad (2.28)$$

M is the number of degenerate mode groups.

In Eqs. (2.27) and (2.28) use has been made of the cut-off condition given in Eq. (2.20). Note that in the case of a single-mode fiber only the first term of the summation in Eq. (2.27) is present, where we have  $m = n = 0$ .

We now apply in Eq. (2.27) the explicit expression for coupling coefficients (2.24):

$$\eta = \sqrt{\kappa_{\perp}\kappa_{\parallel}} \sum_{m=0}^M \frac{(2m)!}{4^m(m!)^2} (1 - \kappa_{\perp})^m$$

$$\times \sum_{n=0}^{M-m} \frac{(2n)!}{4^n(n!)^2} (1 - \kappa_{\parallel})^n, \quad m, n = 0, 1, 2, \dots, M. \quad (2.29)$$

### C. Optimal Laser-to-Fiber Coupling

The laser parameters  $\omega_{\perp}$ ,  $\omega_{\parallel}$  always differ remarkably from the characteristic spot size  $\omega_0$  of the fiber. For this reason it is necessary to have coupling optics for transformation of  $\omega_{\perp}$ ,  $\omega_{\parallel}$  with respect to  $\omega_0$ . Although the laser beam is generally axially nonsymmetric ( $\omega_{\perp} \neq \omega_{\parallel}$ ), rotationally symmetric lenses are the best choice having regard to ease of fabrication. This aspect has been discussed by several authors [14 – 16]. Throughout this section we will assume round thin lenses without aberrations. We start the calculation of the optimum coupling conditions, concerning the focal length and setting relation between laser, lens and fiber, by formulating the physical aspects of the problem.

The optical diagram of this coupling problem is shown in Fig. 2.11. Consider the infinite-parabolic medium, defined by Eq. (2.15), instead of the actual index profile.

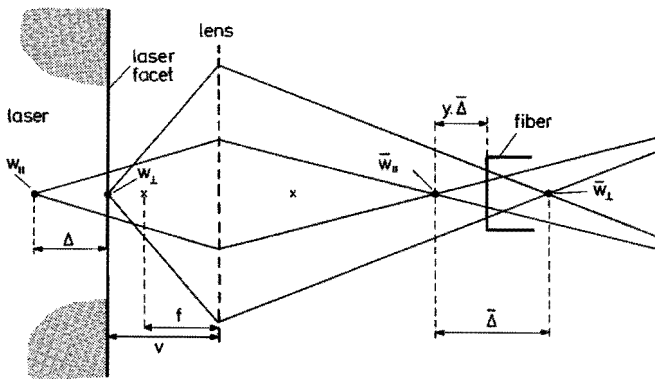


Fig. 2.11 Lens coupling of the light radiated from an astigmatic laser diode into a fiber

A Gaussian beam impinging on the input plane of the medium (corresponding to the fiber endface) gives rise to a Gaussian beam whose contour is a spatial oscillating function, which is shown in Fig. 2.12.

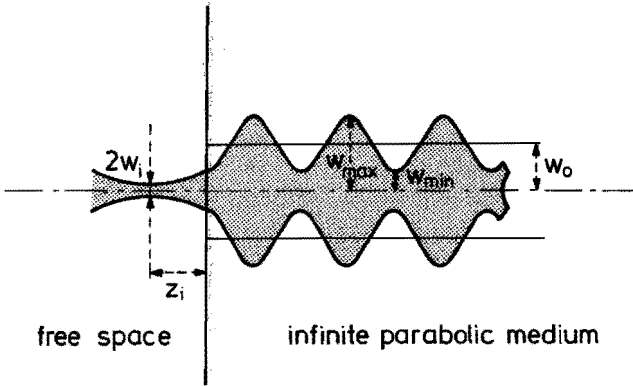


Fig. 2.12 Undulating Gaussian beam in an infinite parabolic medium, which is excited by an incoming Gaussian beam in free space

The maximum and minimum widths of the beam are closely related to each other [17]:

$$\omega_{max} \cdot \omega_{min} = \omega_0^2 \quad (2.30)$$

Assume that the incident beam has a waist  $\omega_i$ , located at a distance  $z_i$  from the input plane. Then (see Appendix C)

$$\left( \frac{\omega_m}{\omega_0} + \frac{\omega_0}{\omega_m} \right)^2 = \left( \frac{\omega_i}{\omega_0} + \frac{\omega_0}{\omega_i} \right)^2 + \left( \frac{2z_i}{k_0 \omega_0 \omega_i} \right)^2, \quad (2.31)$$

offers two solutions for  $\omega_m$ , corresponding to the maximum and the minimum width respectively.

We assume by hypothesis that coupling to a fiber with finite core radius is as high as possible when the minimum radial field extension occurs from the optical axis of the infinite parabolic medium. Considering the oscillating beam only in the plane perpendicular to the junction, one notes that, from Eq. (2.30), the minimum field extension requires  $\omega_{max} = \omega_{min} = \omega_0$ , that is, the incoming beam is perfectly matched to the fundamental mode of the medium. However, in the plane parallel to the junction the corresponding beam will at the same time be mismatched to the fundamental mode, because the incoming laser beam is elliptical and astigmatic. If  $\omega_{max}^\perp$  and  $\omega_{max}^\parallel$  are the solutions of Eq. (2.31) perpendicular and parallel to the junction plane respectively, the minimum field extension is obtained when the condition  $\omega_{max}^\perp = \omega_{max}^\parallel = \text{minimum}$  is fulfilled. This situation is visualized in Fig. 2.13, where projections in a transverse plane of the beam contour are made at subsequent stages along the propagation axis. The smallest enclosing circle is



obtained if the above-mentioned condition is satisfied. In this situation, reduction of  $\omega_{\max}^{\perp}$  gives rise to an increment of  $\omega_{\max}^{\parallel}$  and vice versa. Thus the overall field extension increases as well. Using Eq. (2.31) the mathematical formulation of the above-mentioned conditions is:

$$\left(\frac{\omega_{\perp}}{\omega_0} + \frac{\omega_0}{\omega_{\perp}}\right)^2 + \left(\frac{2z_{\perp}}{k_0 \omega_0 \omega_{\perp}}\right)^2 =$$

$$\left(\frac{\omega_{\parallel}}{\omega_0} + \frac{\omega_0}{\omega_{\parallel}}\right)^2 + \left(\frac{2z_{\parallel}}{k_0 \omega_0 \omega_{\parallel}}\right)^2 = \text{minimum} . \quad (2.32)$$

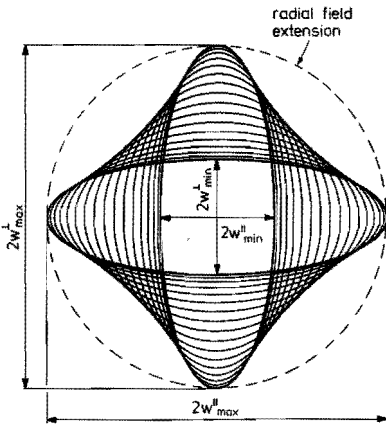


**Fig. 2.13** Projections of the beam contour at subsequent stages along the axis of the infinite parabolic medium at optimum coupling conditions

Investigation of Eqs. (2.32) and (2.25) tells us that maximum coupling efficiency requires

$$\kappa_{\perp} = \kappa_{\parallel} = \kappa_0 . \quad (2.33)$$

In that case Eq. (2.29) reduces to

$$\eta_0 = \kappa_0 \sum_{m=0}^M 4^{-m} (1 - \kappa_0)^m \sum_{n=0}^m \frac{(2n)!}{(n!)^2} \frac{(2m-2n)!}{[(m-n)!]^2} . \quad (2.34)$$

Application of the identity [18]

$$\sum_{n=0}^m \frac{(2n)!}{(n!)^2} \frac{(2m-2n)!}{[(m-n)!]^2} = 4^m , \quad (2.35)$$

leads to an important simplification:

$$\eta_0 = \kappa_0 \sum_{m=0}^M (1 - \kappa_0)^m . \quad (2.36)$$

Summation of the power series in Eq. (2.36) finally gives

$$\eta_0 = 1 - (1 - \kappa_0)^{M+1} . \quad (2.37)$$

As mentioned before, the laser beam and the fundamental fiber mode are strongly mismatched. To achieve the best mode-matching, we use an ideal lens with focal length  $f$ . A beam transformation by such a lens is described by [19].

$$\frac{\omega_{2,1}}{\omega_{1,2}} = \pm \frac{(f^2 - f_0^2)^{1/2}}{d_{1,2} - f} , \quad (2.38)$$

with

$$f_0 = (\pi/\lambda_0) \omega_1 \omega_2 , \quad (2.39)$$

where the quantities have been defined in Fig. 2.14.

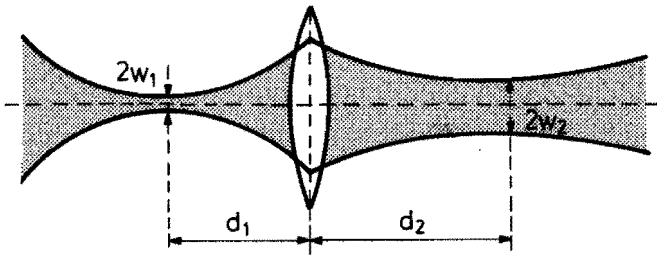


Fig. 2.14 Matching of Gaussian beams by means of a lens

For practical configurations we have only to consider the positive sign in Eq. (2.38). The optimum coupling efficiency can be obtained with a matching lens of arbitrary focal length. It is only required that  $f \geq f_0$ . To calculate the value of the optimum coupling efficiency we choose for convenience  $f \gg f_0$ , which is allowed because the optimum coupling efficiency does not depend on the actual value of  $f$ . The transformation formulas now simplify remarkably:

$$\frac{\bar{\omega}_\perp}{\omega_\perp} = \frac{\bar{\omega}_\parallel}{\omega_\parallel} = \frac{f}{v - f} , \quad (2.40)$$

where  $\bar{\omega}_\perp$  and  $\bar{\omega}_\parallel$  are the transformed beam waists of the laser and  $v$  is the distance from the laser facet to the principal plane of the lens (see Fig. 2.11). Another important aspect of the transformation is its influence on the astigmatism  $\Delta$ . For the transformed astigmatism  $\bar{\Delta}$  one can derive

$$\bar{\Delta} = \frac{f^2}{(v-f)^2} \Delta . \quad (2.41)$$

Optimizing the coupling efficiency requires [compare with Eq. (2.32)]

$$\begin{aligned} \left( \frac{\bar{\omega}_\perp}{\omega_0} + \frac{\omega_0}{\bar{\omega}_\perp} \right)^2 + \left( \frac{2y\bar{\Delta}}{k_0 \omega_0 \bar{\omega}_\perp} \right)^2 = \\ \left( \frac{\bar{\omega}_\parallel}{\omega_0} + \frac{\omega_0}{\bar{\omega}_\parallel} \right)^2 + \left( \frac{2(1-y)\bar{\Delta}}{k_0 \omega_0 \bar{\omega}_\parallel} \right)^2 = \text{minimum} , \end{aligned} \quad (2.42)$$

where the unknown quantity  $y$  introduced in Fig. 2.11 indicates that the best position of the fiber endface will be between the two transformed beam waists. Next, we define

$$x = (v-f) / f , \quad (2.43)$$

$$b = (\lambda_0 \Delta) / (\pi \omega_\perp \omega_\parallel) . \quad (2.44)$$

Insertion of Eqs. (2.43) and (2.44) into Eq. (2.42) gives

$$\begin{aligned} \left( \frac{W_\perp}{x} \right)^2 + \left( \frac{x}{W_\perp} \right)^2 + \left( yb \frac{W_\parallel}{x} \right)^2 = \\ \left( \frac{W_\parallel}{x} \right)^2 + \left( \frac{x}{W_\parallel} \right)^2 + \left[ (1-y)b \frac{W_\perp}{x} \right]^2 = \text{minimum} . \end{aligned} \quad (2.45)$$

The two unknown quantities  $x$  and  $y$  in Eq. (2.45) can be solved by using the following procedure: first,  $x$  is eliminated. We therefore express  $x$  as a function of  $y$ :

$$x^2 = W_\perp W_\parallel \left[ 1 + b^2 \cdot \frac{(1-y)^2 \alpha^2 - y^2}{1 - \alpha^2} \right]^{1/2} , \quad (2.46)$$

where

$$\alpha = \omega_\perp / \omega_\parallel . \quad (2.47)$$

Next, putting

$$\frac{d}{dy} [W_{\perp}^{-2} x^2(y) + (W_{\perp}^2 + b^2 W_{\parallel}^2 y^2) x^{-2}(y)] = 0, \quad (2.48)$$

where  $x(y)$  has been defined by Eq. (2.46), yields an equation for  $y$  only. The solution of Eq. (2.48) is

$$y_0 = \alpha^2 / (1 + \alpha^2). \quad (2.49)$$

The associated value of  $x$  can be obtained by substitution of Eq. (2.49) into Eq. (2.46):

$$x_0^2 = W_{\perp} W_{\parallel} \left[ 1 + \left( \frac{b}{\alpha + \alpha^{-1}} \right)^2 \right]^{\frac{1}{2}}. \quad (2.50)$$

Finally, the optimal coupling factor  $\kappa_0$  with the fundamental mode of the fiber follows from insertion of Eqs. (2.49) and (2.50) into, for example, the left-hand side of Eq. (2.45), which in turn is closely related to Eq. (2.25) of  $\kappa_{\perp, \parallel}$ . The result is

$$\kappa_0 = \frac{4}{2 + (\alpha + \alpha^{-1}) \cdot \left[ 1 + \left( \frac{b}{\alpha + \alpha^{-1}} \right)^2 \right]^{\frac{1}{2}}}. \quad (2.51)$$

The attainable coupling efficiency  $\eta_0$  is determined by application of Eq. (2.51) in Eq. (2.37).

In laser packages with fiber pigtailed it is most convenient to choose the focal length of the matching optics as small as possible for two reasons. First, this keeps the aberration small, because for simple single-element lenses it is proportional to the focal length. Second, the longitudinal alignment condition is then quite simple. For such a lens the laser facet must coincide with the focal plane, so that it need only be adjusted until the divergence in the  $\perp$  plane of the transformed far field reaches its minimum value. According to Eq. (2.38) we then have

$$f = (\pi / \lambda_0) \omega_{\perp} \bar{\omega}_{\perp}. \quad (2.52)$$

Application of the transformation Eqs. (2.38) and (2.39) with  $\omega_{\perp}$  in the focal plane and  $f$  given by Eq. (2.52) results in

$$\bar{\omega}_{\perp} / \omega_{\perp} = b\alpha^{-1} u^{-1} , \quad (2.53)$$

$$\bar{\omega}_{\parallel} / \omega_{\parallel} = u^{-1} [1 + (b\alpha)^{-2}]^{-1/2} , \quad (2.54)$$

$$\bar{\Delta} = u^{-2} [1 + (b\alpha)^{-2}]^{-1} \cdot \Delta , \quad (2.55)$$

where the unknown quantity  $u$  is expressed by

$$u = \Delta / f . \quad (2.56)$$

Using the same method as before, it can be proved that the requirements for maximum coupling efficiency [compare with Eq. (2.42)] are satisfied if

$$y_m = \frac{b^2 + \alpha^{-2}}{1 + b^2 + \alpha^{-2}} , \quad (2.57)$$

$$u_m^2 = \frac{b^2 W_{\parallel}^2}{1 + b^2 + \alpha^{-2}} [(\alpha + \alpha^{-1})^2 + b^2]^{1/2} . \quad (2.58)$$

Here  $u_m$  and  $y_m$  are the counterparts of  $x_0$  and  $y_0$  in Eqs. (2.49) and (2.50) respectively. Using Eqs. (2.57) and (2.58) we can derive exactly the same expression for  $\kappa_0$  as the one given in Eq. (2.51). Insertion of Eq. (2.56) into Eq. (2.58) finally gives

$$f_m^2 = \left( \frac{\pi \omega_{\perp} \omega_0}{\lambda_0} \right)^2 \cdot \frac{b^2 + \alpha^{-1} (\alpha + \alpha^{-1})}{[b^2 + (\alpha + \alpha^{-1})^2]^{1/2}} . \quad (2.59)$$

Note that most of the results obtained in this section are also valid for single-mode fibers. The maximum coupling, for instance, is  $\kappa_0$  given by Eq. (2.51).

#### D. Calculation Examples

Equation (2.51) shows that the maximum fractional power  $\kappa_0$  coupled from the laser beam to the fundamental mode of the fiber depends only on the three geometric parameters of the laser radiation pattern, and the wavelength of emission. These parameters are hidden in the beam ellipticity  $\alpha$  and the level of astigmatism  $b$ . Previous sections have shown that it is convenient to use  $\omega_{\perp, \parallel}$  for the mathematical description instead of  $\theta_{\perp, \parallel}$ , which are usually given for a laser diode. From Eq. (2.12) one can easily derive a simple relation between these two sets of parameters:

$$\omega_{\perp, \parallel} = \frac{\lambda_0 (2 \ln 2)^{1/2}}{2 \pi \tan(\theta_{\perp, \parallel} / 2)} . \quad (2.60)$$

At this point we recall that  $\theta_{\perp,||}$  are the FWHM of intensity of the far field.

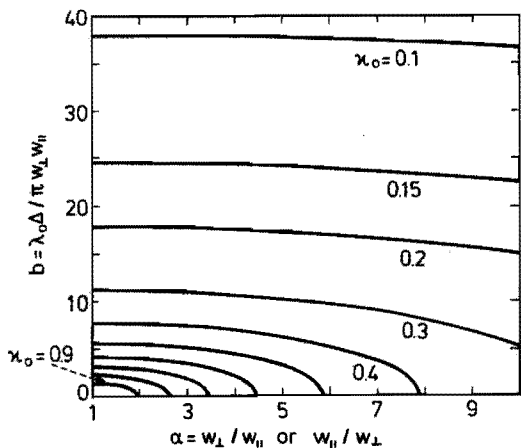


Fig. 2.15 Optimum coupling efficiency between laser and single-mode fiber or fundamental mode of a multimode graded-index fiber

In Fig. 2.15 we have plotted the contours of  $\kappa_0$  as a function of  $\alpha = \omega_{\perp} / \omega_{||}$  and  $b = (\lambda_0 \Delta) / (\pi \omega_{\perp} \omega_{||})$ . These contours of  $\kappa_0$  are predominantly flat with respect to  $\alpha$ , indicating that  $\kappa_0$  is most seriously affected by the astigmatism of a laser. For example, commonly used gain-guided lasers have  $\Delta \cong 20 \mu\text{m}$  (together with  $\theta_{\perp,||} = 55, 20^\circ$  and  $\lambda_0 = 0.83 \mu\text{m}$  leading to  $b \cong 20$ ), allowing a maximum coupling efficiency  $\kappa_0 \cong 0.2$ . On the other hand, an index-guided laser with the same far field, but without astigmatism, gives rise to  $\kappa_0 \cong 0.8$ . Fig. 2.16 illustrates the effect of astigmatism on the maximum coupling efficiency between laser diode and single-mode fiber. It turns out that even a few microns of astigmatism, which can also occur in some types of index-guided lasers [8], already have a noticeable effect.

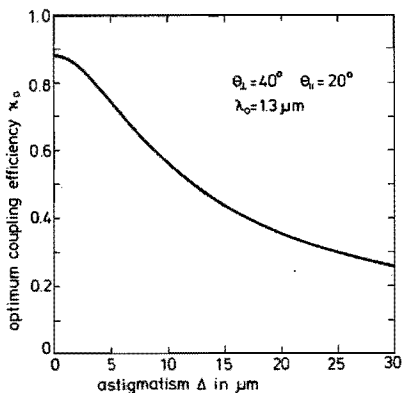


Fig. 2.16 Influence of astigmatism on maximum coupling efficiency between laser and single-mode fiber when keeping far-field parameters constant

Additionally, one notes that gain-guided lasers ( $\Delta \cong 20 \mu\text{m}$ ) are less suitable for light injection in single-mode fibers.

To investigate the influence of the parameters of a multimode graded-index fiber on the maximum overall coupling efficiency  $\eta_0$ , we have to insert a calculated value of  $\kappa_0$  in Eq. (2.37). Fig. 2.17 shows  $\eta_0$  vs the optical throughput  $a \cdot \text{NA}$  of a multimode graded-index fiber for laser diodes with various astigmatisms. The staircase curves

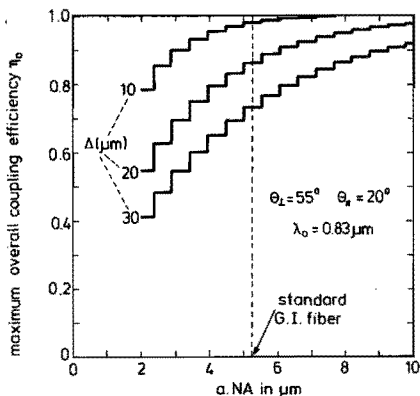


Fig. 2.17 Optimum coupling efficiency between laser and multimode graded-index fiber for some typical gain-guided lasers

emphasize the modal behavior of the fiber. For example, in the standard graded-index fiber ( $a = 25 \mu\text{m}$ ,  $\text{NA} = 0.21$ ) there are ten mode groups propagating. Each jump in the curves means that a (degenerate) mode group has reached its cut-off condition.

We finally note that application of Eq. (2.37) to index-guided lasers ( $\Delta = 0 \mu\text{m}$ ) causes hardly any deviation in  $\eta_0$  from unity when  $a \cdot \text{NA}$  is varied and for this reason it is not indicated in Fig. 2.17.

#### 2.4.2 Lens Coupling between Unequal Fibers

Both multiplexers and demultiplexers can contain lens couplings between unequal fibers. In these devices the input fiber is graded-index, while at the output an oversized graded-index or step-index fiber can be used.

The starting point of the considerations is the model used in chapter 1, where the lens coupling between two identical fibers was studied (see Fig. 1.7). Considering the coupling between unequal fibers, we have to replace the term  $\pi r_1^2(\theta)$  in Eq. (1.18) by the relative overlap  $O$  of two circles with radii  $r_1(\theta)$  and  $r_2(\theta)$ , respectively, whose centers are separated by a distance  $\epsilon(\theta)$ , the spherical aberration.  $r_2(\theta)$  is the counterpart of  $r_1(\theta)$  for the receiving fiber.

Putting

$$x = \sin\theta / NA , \quad (2.61)$$

$$y = \varphi / 2\pi , \quad (2.62)$$

we can express the coupling efficiency by

$$\eta = 4 \int_0^1 \int_0^1 O(x,y) x (1 - x^2) dx dy . \quad (2.63)$$

(parabolic index profile).

In Eq. (2.63) the overlap was taken relative to the emitting circle with radius  $r_1(\theta)$ , given by

$$r_1(\theta) = a (1 - x^2)^{1/2} , \quad (2.64)$$

where use has been made of Eqs. (1.16) and (2.61).

Next we consider the overlap function  $O(x, y)$  taking into account the exact ray trajectories.

In this description  $O(x, y)$  represents the fractional area of the circle at the emitting fiber that contributes to the lens coupling. The boundary of this fractional area, from which all emitted rays are accepted at the output, depends in a complicated way on the ray angles  $\theta$  and  $\varphi$ . For this reason we used a quasi-Monte Carlo method to calculate  $O(x, y)$ . In this method the circle is covered by a set of points at which the rays are launched. Counting the number of rays that are accepted and the number of all rays that are launched yields, after division of both numbers, an approximate value of  $O(x, y)$ . We constructed the lattice points from the Fibonacci numbers, because for 2-D areas such a sequence of points is the best choice [20]. Finally, the two-fold integration in Eq. (2.63) is carried out by using a product rule of two Gaussian quadratures of equal order.



## APPENDIX C

In a medium whose refractive index is given by

$$n(x) = n_0 [1 - g^2(z)x^2]^{1/2}, \quad (C1)$$

the Gaussian beam

$$u(x, z) = q^{-1/2}(z) \exp\left[\frac{i}{2} k_0 \dot{q}(z) q^{-1}(z)x^2\right] \exp(ik_0 z) \quad (C2)$$

is in very good approximation a solution of the scalar wave equation, if the complex beam parameter  $q(z)$  satisfies [17]

$$\ddot{q}(z) + g^2(z)q(z) = 0. \quad (C3)$$

The dot means differentiation with respect to  $z$ .

At the boundary,  $z=\text{constant}$ , between free space [ $g(z) \equiv 0$ ] and an infinite parabolic medium [ $g(z) \equiv \text{positive constant}$ ] the transverse components must be continuous.

From Eq. (C2) we see that this boundary condition requires

$$\dot{q}_{\text{in}}(z) \cdot q_{\text{in}}^{-1}(z) = n_0 \dot{q}_{\text{f}}(z) \cdot q_{\text{f}}^{-1}(z) \quad (C4)$$

at the input plane of the fiber.

The free-space solution  $q_{\text{in}}(z)$  is given by

$$q_{\text{in}}(z) = \omega_i \left(1 + i \cdot \frac{2z}{k_0 \omega_i^2}\right). \quad (C5)$$

For the parabolic medium we have

$$q_{\text{f}}(z) = \omega_m \cos(gz) + i \cdot \frac{\omega_0^2}{\omega_m} \sin(gz). \quad (C6)$$

By inserting Eqs. (C5) and (C6) into Eq. (C4) and equating the real and imaginary parts we obtain two coupled equations for  $\omega_m$  and its location  $z_m$ . Elimination of  $z_m$  then finally gives Eq. (2.31).

## REFERENCES

1. W.J. Tomlinson, *Appl. Opt.* 16, 2180 (1977).
2. G.D.Khoe, in *Technical Digest, Seventh ECOC, Copenhagen (1981)*, p.16.2-1.
3. K. Aiki et al., *Appl. Phys. Lett.* 29, 506 (1976).
4. S. Sakai et al., *Appl. Phys. Lett.* 35, 588 (1979).
5. J.C. Campbell et al., *IEEE J. Quantum Electron.*, QE-16, 601 (1980).
6. S. Sakai et al., *Trans. Inst. Electron. Commun. Eng. Jpn.* 63-E, 192 (1980).
7. P. di Vita and C. so Francia, *Patent Application 79100314.8*, (1979).
8. K. Tatsuno and A. Arimoto, *Appl. Opt.* 20, 3520 (1981).
9. T.P. Lee et al., *Electron. Lett.* 18, 902 (1982).
10. H.W. Kogelnik and T. Li, *Appl. Opt.* 5, 1550 (1966).
11. D. Marcuse, *Light Transmission Optics*, (Van Nostrand-Reinhold, New York, 1972), p. 270.
12. D. Marcuse, *Bell Syst. Tech. J.* 52, 1169 (1973).
13. H. Kogelnik, *Coupling and Conversion Coefficients for Optical Modes*, Vol. 14, *Microwave Research Institute Symposia Series*, J. Fox, Ed. (Polytechnic Press, Brooklyn, 1964), p. 333.
14. G.D. Khoe et al., in *Digest of Topical Meeting on Optical Fiber Communication (Optical Society of America, Washington, D.C., 1979)*, paper TnB6.
15. J. Yamada et al., *IEEE J. Quantum Electron.* QE-16, 1067 (1980).
16. M. Saruwatari and T. Sugie, *Electron. Lett.* 16, 955 (1980).
17. J.A. Arnaud, *Beam and Fiber Optics*, (Academic Press, New York, 1976), p. 65.
18. C.L. Liu, *Introduction to Combinatorial Mathematics*, (McGraw-Hill, New York, 1968), p. 30.
19. H.W. Kogelnik, *Bell Syst. Tech. J.* 44, 455 (1965).
20. S.K. Zarembo, *Ann. Mat. Pura Appl.* 73, 293 (1966).

### 3. DESIGN AND CONSTRUCTION OF MULTIPLEXERS

#### 3.1 Introduction

The optical arrangements of two promising types of wavelength-independent multiplexers are discussed in this chapter: a structure without lenses, which we name butt-joint multiplexer, and a structure using lenses, referred to as a prism multiplexer. Based on the same principles more structures are possible, but in all of them spatial filtering is essential.

In addition, the minimization of the overall transmitter end loss of a WDM system is dealt with. For this it is necessary to combine the transmission properties of the above-mentioned multiplexers with laser/LED-fiber coupling efficiencies, derived in chapter 2.

#### 3.2 Butt-Joint Multiplexer

##### 3.2.1 Theory according to the Intensity Law

The structure of a two-channel multiplexer is illustrated in Fig. 3.1, where only the bare fibers are shown. Both input fibers are provided with a longitudinal polishing plane making an angle of typically  $1.5^\circ$  with the fiber axis, and second, a transverse polishing plane perpendicular to the longitudinal one. When two such input fibers are composed, and butt-joined to the output fiber, we have the geometry shown in Fig. 3.2 at the junction. At present we adopt a simplified model for the calculation of the insertion loss of this multiplexer, i.e. the insertion loss is assumed to be the relative amount of light in the fiber cross-section that was removed during polishing (see also Fig. 3.2).

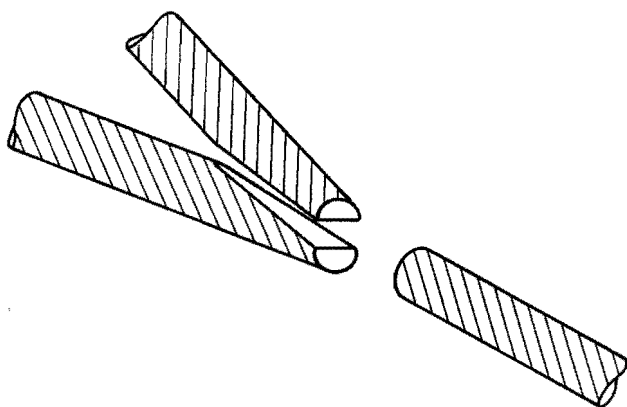


Fig. 3.1 Structure of the butt-joint multiplexer

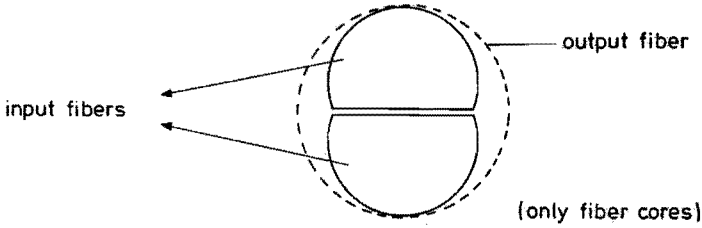


Fig. 3.2 Cross-section at the junction of the fibers of the two-channel multiplexer

For the loss factor  $F(\varphi)$ , which is the relative amount of light in the shadowed circle segment with respect to the light in the entire cross-section (see Fig. 3.3), we have

$$\begin{aligned}
 F(\varphi) &= \frac{1}{\pi} \left\{ \varphi + \left(\frac{d}{a_i}\right)^2 \left[ \frac{1}{3} \left( \frac{1}{\cos^2 \varphi} + 2 \right) \left(\frac{d}{a_i}\right)^2 - 2 \right] \tan \varphi \right\}, \quad d \leq a_i, \\
 &= 0, \quad d > a_i,
 \end{aligned}
 \tag{3.1}$$

where  $a_i$  is the core radius of the input fibers, and  $d, \varphi$  are geometrical parameters defined in Fig. 3.3. In deriving Eq. (3.1) it has been assumed that the index profile is parabolic and that we have uniform launching conditions. Details of the derivation can be found in Ref. 1. Keeping in mind the cross-section shown in Fig. 3.2, it can easily be seen that the transmission coefficient  $T$  of one channel of the multiplexer is

$$T = 1 - F[\arccos(d/a_i)], \quad \text{if } d = a_0 - a_i, \tag{3.2}$$

where  $a_0$  is the core radius of the output fiber.

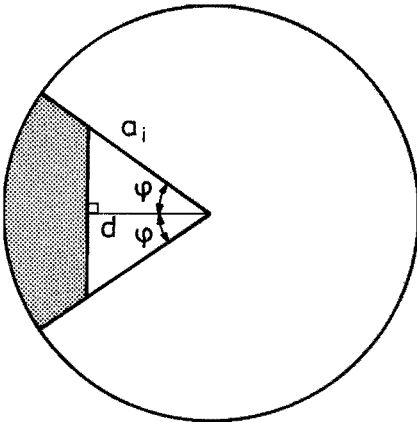


Fig. 3.3 Visualization of the loss factor, which is the relative amount of light in the shadowed circle segment

Using only geometrical considerations, the loss factor  $F(\varphi)$  can be applied to multiplexers with an arbitrary number of channels. The transmission coefficient of such a multiplexer is

$$T = 1 \quad , \quad a_i \leq d \quad ,$$

$$T = 1 - 2F[\arccos(d/a_i)] \quad , \quad d < a_i \leq a_0/2 \quad , \quad (3.3)$$

$$T = 1 - F[\arccos(d/a_i)] - F\left(\frac{N-2}{N} \frac{\pi}{2}\right) \quad , \quad a_0/2 < a_i \leq a_0 \quad ,$$

where

$$d = (a_0 - a_i) \sin(\pi/N) \quad , \quad (3.4)$$

$N$  is the number of channels. In Fig. 3.4 we show a four-channel structure for a better understanding of Eqs. (3.3) and (3.4). From these equations it follows that loss-free operation requires

$$a_i \leq a_0 \cdot \frac{\sin(\pi/N)}{1 + \sin(\pi/N)} \quad . \quad (3.5)$$

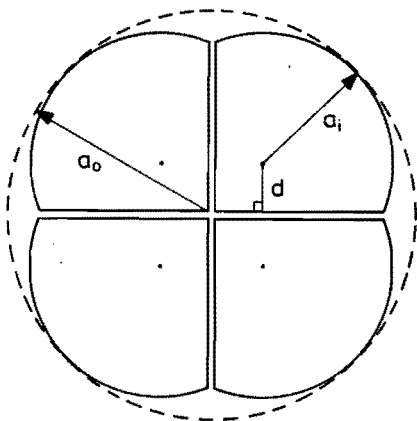


Fig. 3.4 Cross section of a four-channel butt-joint multiplexer

In addition to the loss mechanism described above we have a mismatch in the local numerical apertures. This mismatch does not cause any loss if

$$NA_i \leq (a_i / a_0)^{1/2} NA_0 \quad , \quad (3.6)$$

where  $NA_1$  and  $NA_0$  are the on-axis numerical apertures of the input fibers and output fiber respectively.

The combination of Eq. (3.5) with the equal sign, and Eq. (3.6) finally gives

$$a_1 NA_1 \leq a_0 NA_0 \left[ \frac{\sin(\pi/N)}{1 + \sin(\pi/N)} \right]^{3/2} \quad (3.7)$$

It should be noted that condition (3.7) is stricter than the fundamental limit (2.4). For example, a four-channel structure would require  $a_1 NA_1 / a_0 NA_0 < 0.27$  according to (3.7) instead of the 0.5 value that follows from the fundamental limit. However, a closer approach to this fundamental limit would require noncircular fibers. Note that from physical reasoning the multiplexer is affected by the tilt angle between the axes of the fibers to be combined. However, from a theoretical point of view this tilt angle can be made arbitrarily small. For this reason it is not taken into account in this simplified model, but it is in the next section.

### 3.2.2 Theory according to Ray-Tracing

The analysis starts with the determination of ray trajectories in an unperturbed graded-index fiber. The basic equation for all possible ray trajectories in a medium with a certain index distribution is written in vectorial form as [2]

$$\frac{d}{ds} \left( n \frac{d\mathbf{R}}{ds} \right) = \text{grad } n \quad (3.8)$$

where  $\mathbf{R} = \mathbf{R}(s)$  is a position vector of a typical point on a ray and  $s$  the length of the ray measured from a fixed point on it. As a graded-index fiber has a radial index distribution  $n$  and a dielectric constant  $n^2$ , which is a quadratic function of the radial distance  $r$  from the axis, it is best to adopt Cartesian coordinates  $(x, y, z)$  with the  $z$ -axis chosen along the fiber axis [3]. Eq. (3.8) is now rewritten in terms of its vector components:

$$\cos\theta \frac{d}{dz} \left( n \cos\theta \frac{dx}{dz} \right) = \frac{\partial n}{\partial x} \quad (3.9)$$

$$\cos\theta \frac{d}{dz} \left( n \cos\theta \frac{dy}{dz} \right) = \frac{\partial n}{\partial y} \quad (3.10)$$

$$\frac{d}{dz} (n \cos\theta) = 0 \quad (3.11)$$

where the derivatives with respect to  $s$  are converted to derivatives in  $z$ , using the angle  $\theta$  between the fiber axis and the ray.

Eq. (3.11) shows at once that

$$n \cos\theta = M_0 = \text{constant} . \quad (3.12)$$

Thus, with the optical direction cosines  $K, L, M$ , defined as the product of the refractive index and the geometrical direction cosines at a typical point on a trajectory, Eq. (3.12) shows that the third optical direction cosine is invariant along any ray,  $M=M_0$ .

After multiplication of both sides of Eqs. (3.9) and (3.10) by  $n$  and using Eq. (3.12) we can reduce these equations to

$$M_0^2 \frac{d^2 x}{dz^2} = \frac{1}{2} \frac{\partial n^2}{\partial x} , \quad (3.13)$$

$$M_0^2 \frac{d^2 y}{dz^2} = \frac{1}{2} \frac{\partial n^2}{\partial y} . \quad (3.14)$$

The index profile of the fiber core is described by

$$n^2 = n_{cl}^2 + NA_i^2 \left( 1 - \frac{x^2}{a_i^2} - \frac{y^2}{a_i^2} \right) , \quad x^2 + y^2 \leq a_i^2 , \quad (3.15)$$

where  $n_{cl}$  is the refractive index of the cladding,  $a_i$  is the core radius, and  $NA_i$  is the on-axis numerical aperture.

Insertion of Eq. (3.15) into Eqs. (3.13) and (3.14) gives

$$\frac{d^2 x}{dz^2} + \left( \frac{NA_i}{M_0 a_i} \right)^2 x = 0 , \quad (3.16)$$

$$\frac{d^2 y}{dz^2} + \left( \frac{NA_i}{M_0 a_i} \right)^2 y = 0 . \quad (3.17)$$

At this stage we introduce a normalization: all lengths are expressed relative to the core radius  $a_i$ , and the optical direction cosines are taken relative to the numerical aperture  $NA_i$ . These normalized quantities are provided with a bar above the original symbol.

With this normalization, the solution of Eqs. (3.16) and (3.17) is given by

$$\bar{x} = \bar{x}_m \sin(\bar{\Omega} \bar{z} + \psi_x) , \quad (3.18)$$

$$\bar{y} = \bar{y}_m \sin(\bar{\Omega} \bar{z} + \psi_y) , \quad (3.19)$$

with

$$\bar{\Omega} = \bar{M}_0^{-1} , \quad (3.20)$$

$$\bar{x}_m = (\bar{x}_0^2 + \bar{K}_0^2)^{1/2} , \quad (3.21)$$

$$\bar{y}_m = (\bar{y}_0^2 + \bar{L}_0^2)^{1/2} , \quad (3.22)$$

$$\tan\psi_x = \bar{x}_0 / \bar{K}_0 , \quad (3.23)$$

$$\tan\psi_y = \bar{y}_0 / \bar{L}_0 , \quad (3.24)$$

where  $\bar{x}_0, \bar{y}_0, \bar{K}_0, \bar{L}_0$  are the values of  $\bar{x}, \bar{y}, \bar{K}, \bar{L}$  respectively when  $\bar{z} = 0$ . The phase angles  $\psi_x$  and  $\psi_y$  are defined such that they are in the interval  $(0, 2\pi)$ . The optical direction cosines at a general point of the ray are found by differentiation of Eqs. (3.18) and (3.19), for

$$\bar{K} = n \frac{d\bar{x}}{d\bar{s}} = \bar{M}_0 \frac{d\bar{x}}{d\bar{z}} . \quad (3.25)$$

Hence

$$\bar{K} = \bar{x}_m \cos(\bar{\Omega} \bar{z} + \psi_x) , \quad (3.26)$$

$$\bar{L} = \bar{y}_m \cos(\bar{\Omega} \bar{z} + \psi_y) . \quad (3.27)$$

We finally note that  $\bar{K}_0, \bar{L}_0, \bar{M}_0$  have to be determined from the launching conditions at the fiber input plane ( $\bar{z} = 0$ ) at the point  $(\bar{x}_0, \bar{y}_0)$ . The ray is incident at an angle  $\theta_1$  with the fiber axis, and its projection on the input plane has an angle  $\varphi_1$  to the x-axis. Use of Snells law at the interface results in

$$\bar{K}_0 = \overline{\sin\theta}_1 \cos\varphi_1 , \quad (3.28)$$

$$\bar{L}_0 = \overline{\sin\theta}_1 \sin\varphi_1 , \quad (3.29)$$

$$\bar{M}_0 = [ (n_{cl} / NA_1)^2 + 1 - \bar{x}_0^2 - \bar{y}_0^2 - (\overline{\sin\theta}_1)^2 ]^{1/2} . \quad (3.30)$$



With the help of Fig. 3.5 we will now proceed with the geometrical description of the configuration of a two-channel butt-joint multiplexer. The input fibers are provided with two perpendicular planes (I and II in Fig. 3.5). The longitudinal plane I has an angle  $\alpha$  to the fiber axis, while the normals of both planes are in the  $x,z$ -plane. Furthermore, the amount of polishing is described by the parameter  $d$ , defined in Fig. 3.5. For the section length  $z_1$  of the perturbed fiber we have

$$\bar{z}_1 = (1 - \bar{d} \cdot \cos\alpha) / \tan\alpha, \quad \bar{d} \geq 0. \quad (3.31)$$

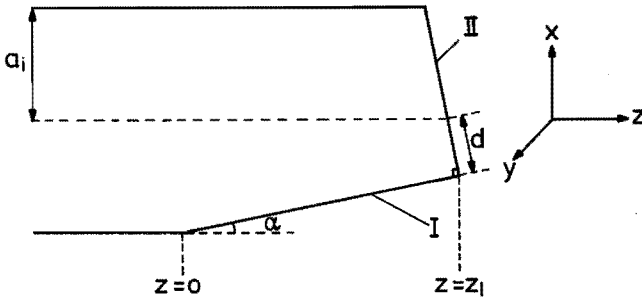


Fig. 3.5 Geometry of a polished input fiber in a two-channel butt-joint multiplexer

A ray striking the longitudinal plane I will continue its propagation in the other input fiber (see Fig. 3.6). As both input fibers have the longitudinal plane in common, no refraction of the ray occurs. It is only necessary to express the intersection point and the corresponding optical direction cosines in terms of the coordinates connected with the other input fiber. The required coordinate transformation for this is equivalent to the change which would take place in ray parameters if total reflection at the common plane in the first fiber occurred.

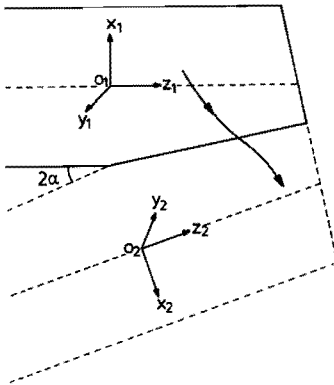


Fig. 3.6 Composition of two polished input fibers

With this equivalency we mean that final acceptance by the output fiber is not influenced by whether the common boundary is mirrored or not. Because of the simpler geometrical interpretation we shall assume that the longitudinal plane is a perfect mirror, and so we have only to consider the propagation in one single (perturbed) fiber.

At each intersection we have to replace

$$\bar{K} \longrightarrow -\bar{K} \cos(2\alpha) + \bar{M} \sin(2\alpha) , \quad (3.32)$$

$$\bar{M} \longrightarrow \bar{K} \sin(2\alpha) + \bar{M} \cos(2\alpha) , \quad (3.33)$$

whereas  $\bar{L}$  remains unchanged.

In the investigation of the first intersection, several possibilities have to be distinguished:

- (1) The amplitude  $\bar{x}_m$  of the spatial oscillation in the x-direction is so small that no intersection with the longitudinal plane is possible.
- (2) The initial phase  $\psi_x$  in Eq. (3.18) is such that intersection with the transverse plane (II in Fig. 3.5) occurs before this would be possible with the longitudinal one. This situation can only happen if the section length  $z_1$  of the perturbed fiber is smaller than the undulation period of the ray.
- (3) Finally, intersection with the longitudinal plane takes place.

It should be noted that calculation of the intersection point leads to the problem of solving a transcendental equation of the type  $\sin(x) = 1 - x$ , which has to be done numerically.

After reflection of the ray at the longitudinal plane its parameters will be changed. Three different kinds of ray continuation are then possible:

- (1) The ray is reflected again at the longitudinal plane.
- (2) The ray reaches the cladding before striking the transverse plane.
- (3) The ray impinges on the transverse plane within the core.

First of all we have to check if the ray can leave the core after reflection. For this purpose we express the distance  $r$  from the ray path to the fiber axis as a function of  $z$

$$\bar{r}^2 = \bar{x}_m^2 \sin^2 [\bar{\Omega}(z - z_s) + \psi_x] + \bar{y}_m^2 \sin^2 [\bar{\Omega}(z - z_s) + \psi_y] , \quad (3.34)$$

where  $\bar{\Omega}$ ,  $\bar{x}_m$ ,  $\bar{y}_m$ ,  $\psi_x$ ,  $\psi_y$  are given by Eqs. (3.20) – (3.24) in combination with the new initial conditions (3.32) and (3.33).

It should be noted that all the ray parameters just mentioned are now determined at the reflection point  $z_s$ .

With some goniometric manipulation we rewrite Eq. (3.34)

$$\bar{r}^2 = \bar{x}_m^2 + \bar{y}_m^2 - [(\bar{x}_m^2 + \bar{y}_m^2)^2 - 4\bar{x}_m^2\bar{y}_m^2\sin^2(\psi_x - \psi_y)]^{1/2} \\ \times \cos[2\bar{\Omega}(\bar{z} - \bar{z}_s) + \psi_r] , \quad (3.35)$$

with

$$\tan\psi_r = [\bar{x}_m^2\sin(2\psi_x) + \bar{y}_m^2\sin(2\psi_y)] / [\bar{x}_m^2\cos(2\psi_x) + \bar{y}_m^2\cos(2\psi_y)] . \quad (3.36)$$

The projection of the ray path in the x, y-plane is given by Eqs. (3.18) and (3.19), which are the parametric equations of an ellipse. The major axis of this ellipse follows from Eq. (3.35)

$$2\bar{r}_{\max}^2 = \bar{x}_m^2 + \bar{y}_m^2 + [(\bar{x}_m^2 + \bar{y}_m^2)^2 - 4\bar{x}_m^2\bar{y}_m^2\sin^2(\psi_x - \psi_y)]^{1/2} . \quad (3.37)$$

A ray can leave the core only if  $\bar{r}_{\max} > 1$ . In that case we put  $\bar{r} = 1$  on the left-hand side of Eq. (3.35) to determine the location  $\bar{z}_c$  at which the ray reaches the core-cladding boundary. So one has to solve  $\bar{z}_c$  from

$$\cos[2\bar{\Omega}(\bar{z}_c - \bar{z}_s) + \psi_r] = \frac{\bar{x}_m^2 + \bar{y}_m^2 - 2}{[(\bar{x}_m^2 + \bar{y}_m^2)^2 - 4\bar{x}_m^2\bar{y}_m^2\sin^2(\psi_x - \psi_y)]^{1/2}} . \quad (3.38)$$

Another requirement for a ray travelling in the cladding is that it has to reach the core-cladding boundary earlier than the transverse plane. If  $\bar{x}_c$  is the corresponding x-coordinate to  $\bar{z}_c$  then the condition

$$\bar{z}_c < \bar{z}_1 - \bar{d} \cdot \sin\alpha - \bar{x}_c \tan\alpha \quad (3.39)$$

has to be satisfied for a ray to leave the core.

Due to the fact that the longitudinal plane is entirely below the y, z-plane we note that if  $\bar{r}_{\max} > 1$  it is impossible for a ray to have another intersection with this longitudinal plane. This is because  $\bar{r}_{\max}$  is always reached first. When  $\bar{r}_{\max} < 1$  we have a situation similar to the determination of the first intersection with the longitudinal plane. As only two ray continuations are possible:

(1) the ray has another intersection with the longitudinal plane,

(2) the ray impinges on the transverse plane within the core,

it is, however, slightly simpler than the first intersection. In case of another intersection the procedure is repeated for the successive intersections until the ray reaches the transverse plane or the core-cladding boundary.

We finally note that calculation of the intersection point with the transverse plane

within the core again leads to a numerical solution of a transcendental equation of the type  $\sin(x) = 1 - x$ . Intersection with the transverse plane in the cladding can easily be calculated analytically, because the ray path is a straight line.

A ray leaving the core through the core-cladding boundary can reach the longitudinal plane in the cladding. It is, however, impossible for the ray to re-enter the core after reflection. We shall show this by geometrical considerations (see also Fig. 3.7).

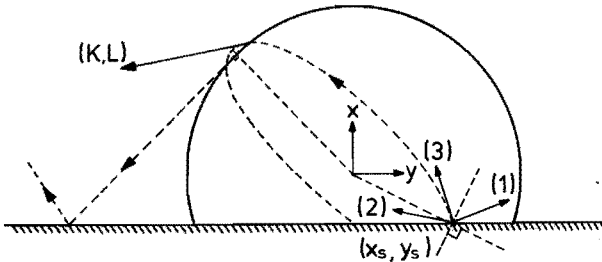


Fig. 3.7 Possible ray continuations after reflection at the longitudinal plane

When the ray leaves the core, three ray continuations have to be considered:

- (1) The initial direction is such that the ray travels first towards the major axis of the ellipse. From the point  $(x_s, y_s)$  until  $r_{\max}$  is reached we have  $K > 0$ , and so no reflection is possible.
- (2) The initial direction is such that the ray travels first towards the minor axis of the ellipse. From the point  $(x_s, y_s)$  until  $r_{\max}$  is reached we have  $K > 0$ , and so no reflection is possible.
- (3) The initial direction is such that the ray travels first towards the minor axis of the ellipse. In some cases it is possible that  $K < 0$  when the ray leaves the core. As the longitudinal plane is entirely below the  $y, z$ -plane,  $r_{\max}$  is always reached above this plane for the first time. The circle describing the core-cladding boundary has in this region (above the point where the major axis intersects the circle) a tangent which travels away from the  $x, z$ -plane when going closer to the longitudinal plane. From Fig. 3.7 we can conclude that after reflection the ray can never be directed towards the core.

To provide a better overview of all possible ray continuations, we have summarized the results of this section in the flow chart in Fig. 3.8.

By means of the previous considerations and calculations, the position and direction of a ray at the transverse plane of the input fiber are known. At this stage it is possible to investigate the acceptance of the ray by the output fiber. This output fiber has a core radius  $a_0$ , and an on-axis numerical aperture  $NA_0$ . For this fiber,

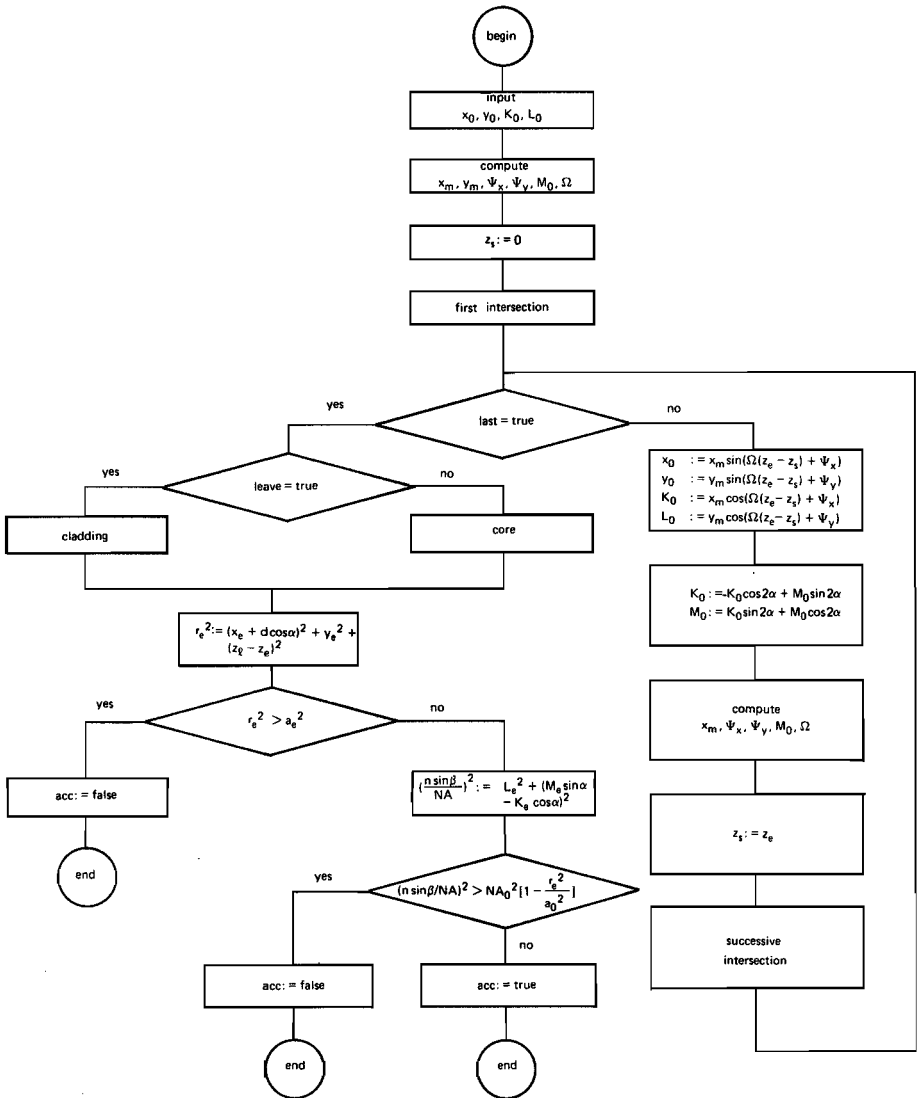


Fig. 3.8 Investigation of ray acceptance by the output fiber

too, the index profile is described by Eq. (3.15). The center of the endface of the output fiber has the coordinates  $(-\bar{d} \cdot \cos\alpha, 0, \bar{z}_1)$ , whereas the ray intersects the transverse plane at  $(\bar{x}_e, \bar{y}_e, \bar{z}_e)$ . The first requirement for acceptance is that the ray should arrive at the output fiber core. This condition can be formulated as

$$\bar{r}_e^2 = (\bar{x}_e + \bar{d} \cdot \cos\alpha)^2 + \bar{y}_e^2 + (\bar{z}_1 - \bar{z}_e)^2 \leq \bar{a}_0^2 . \quad (3.40)$$

Second, the ray direction should be within the local numerical aperture. We note that the axis of the output fiber coincides with the normal of the transverse plane given by  $(\sin\alpha, 0, \cos\alpha)$ . The angle  $\beta$  of the ray with this normal is found from the cross product

$$n \sin\beta = | | (K_e, L_e, M_e) \times (\sin\alpha, 0, \cos\alpha) | | . \quad (3.41)$$

In terms of normalized quantities we have

$$(n \sin\beta)^2 = \bar{L}_e^2 + (\bar{M}_e \sin\alpha - \bar{K}_e \cos\alpha)^2 . \quad (3.42)$$

As  $n \cdot \sin\beta$  does not change during the passage of the transverse plane, we have for the second and final check for acceptance

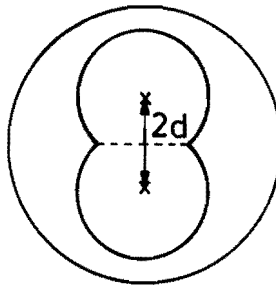
$$(n \sin\beta)^2 \leq \bar{NA}_0^2 [ 1 - (\bar{r}_e / \bar{a}_0)^2 ] , \quad (3.43)$$

where the right-hand side of (3.43) represents the local numerical aperture.

According to the flow chart in Fig. 3.8 we constructed a computer program for the ray-tracing in a two-channel butt-joint multiplexer. This ray-tracing program was used for the numerical calculation of the insertion loss of the above-mentioned multiplexer.

We checked the validity of the simplified model described in section 3.2.1 using the numerical calculations of this section. The comparison of both methods was made for a multiplexer having input fibers with a core diameter of  $33 \mu\text{m}$  and a numerical aperture 0.24. For the output fiber these parameters are  $50 \mu\text{m}$  and 0.26 respectively. As a matter of fact we used such fibers in our experiments, which will be discussed later on. Table 3.1 lists the numerical results of a multiplexer with a polishing angle of  $1.5^\circ$  of the longitudinal plane. We see that for the configuration given in Fig. 3.2 (corresponding to  $2d = 17 \mu\text{m}$ ) the discrepancy between the models is only 1.4%. When more of the cross-section is removed two opposite trends will appear. First, the mismatch between the local numerical apertures will become less, which results in a decrease of the loss. Second, more rays intersect the longitudinal plane, causing a possible increase in loss. From Table 3.1 we see that removing more from the fiber cross-section than in the design according to the simplified model results in a slightly lower insertion loss (optimum at  $2d = 13 \mu\text{m}$ ).

2d ( $\mu\text{m}$ )	efficiency
21	0.859
19	0.883
17	0.895
15	0.908
13	0.911
11	0.910
9	0.904
7	0.891
5	0.873
3	0.845
1	0.825



$$\alpha = 1.5^\circ$$

approximation : 0.882

$$a_1 = 16.5 \mu\text{m}$$

$$a_0 = 25 \mu\text{m}$$

*Table 3.1 Numerical results for a multiplexer with a polishing angle of  $1.5^\circ$*

This can be explained by the fact that the undulation period of the ray is about twice the section length of the perturbed input fiber. Therefore, many rays leaving the input core can still reach the output core. For this reason the first trend, less mismatch in local numerical apertures, has slightly more influence.

In Table 3.2 similar results are listed for a polishing angle of  $0.1^\circ$ . For such a smooth transition we see that there is hardly any deviation between exact ray-tracing and the simplified model of the previous section.

2d ( $\mu\text{m}$ )	efficiency
21	0.847
19	0.871
17	0.878
15	0.880
13	0.859

$$\alpha = 0.1^\circ$$

approximation : 0.882

*Table 3.2 Numerical results for a multiplexer with a polishing angle of  $0.1^\circ$*

### 3.2.3 Overall Transmitter End Loss of a WDM-system

It was pointed out that the transmission of one channel of a butt-joint multiplexer, under uniform launching conditions at the input, is described satisfactorily by Eqs. (3.3) and (3.4). In Fig. 3.9 this transmission is plotted against the ratio  $a_1/a_0$  with the number of channels as the parameter. Although low-loss multiplexers

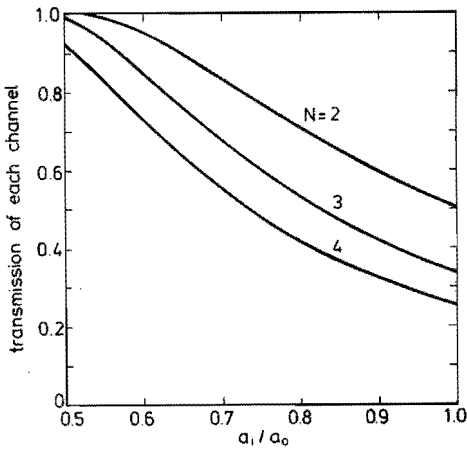


Fig. 3.9 Efficiency curves of two-, three-, and four-channel wavelength-independent multiplexers at uniform launching conditions

can be conveniently constructed, we have to combine the transmission curves of Fig. 3.9 with laser/LED-fiber coupling efficiencies, described by Eqs. (2.1) or (2.55), respectively, to choose a proper  $a_i$  and  $NA_i$ .

As we have already seen, both the above-mentioned coupling efficiencies depend on the optical throughput  $a_i NA_i$  of the fiber. When  $a_i/a_0$  is varied, this optical throughput is maximum if the equal sign is taken in Eq. (3.6). In that case we have

$$a_i NA_i = a_0 NA_0 (a_i/a_0)^{3/2} \quad (3.44)$$

In this section we present transmitter end losses of systems incorporating (1) LEDs, (2) index-guided lasers, (3) gain-guided lasers, in combination with a butt-joint multiplexer.

(1) Consider a top-emitting LED with an emitting area equal to the core of the output graded-index fiber, which is standard  $50 \mu\text{m}$ , and a numerical aperture of unity, as it emits in a hemisphere. For such a LED the coupling efficiency with the input fiber of the multiplexer is given by

$$\eta_{\text{led}} = 0.5 (a_i/a_0)^3 NA_0^2 \quad (3.45)$$

where use has been made of Eqs. (2.1) and (3.44).

The overall insertion loss at the transmitter end when using LEDs is shown in Fig. 3.10. From this figure we see that there are no advantages in using undersized input fibers. Consequently, it is preferable for multiplexing LED signals to be done by wavelength-selective devices. Due to the large wavelength separation present in LED systems, the insertion loss of interference filter multiplexers can be expected to be much lower than the  $10 \log N$  dB inherent in wavelength-independent multiplexing.



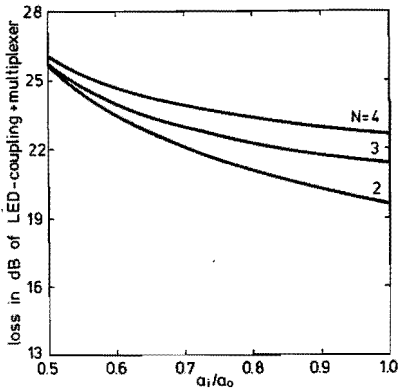


Fig. 3.10 Overall insertion loss at the transmitter end of a WDM system using LEDs depending on the pigtail core radius  $a_i$

(2) A completely different situation is found with a WDM system using index-guided lasers (Fig. 3.11). Here channel attenuations down to 1.5 dB at the transmitter end are possible if four channels with pigtails of  $30 \mu\text{m}$  ( $a_i/a_0 = 0.6$ ), which are still easy to handle, have to be multiplexed. In practice, the curves will even be flatter, closer to the 0-dB axis, because such lasers certainly do not cause a uniform distribution in the pigtails.

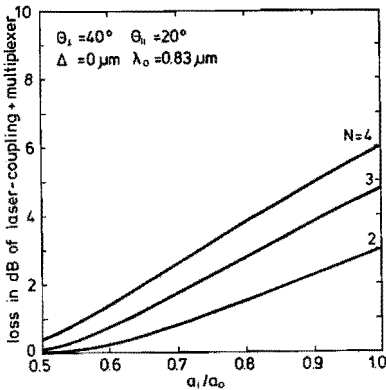


Fig. 3.11 Overall insertion loss at the transmitter end of a WDM system using a typical index-guided laser depending on the pigtail core radius  $a_i$

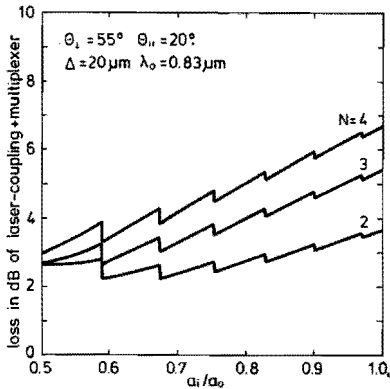


Fig. 3.12 Overall insertion loss at the transmitter end of a WDM system using a typical gain-guided laser depending on the pigtail core radius  $a_1$

(3) Finally, in Fig. 3.12 we show the set of curves when typical gain-guided lasers are incorporated. This situation is intermediate between the ones shown in Figs. 3.10 and 3.11. Here a general answer cannot be given to the question: wavelength-independent multiplexing or not? Before making a choice, the number of channels and the wavelength separation must be considered.

As discussed in the section dealing with the laser-to-fiber coupling, we see that the mode cut-offs in Fig. 3.12 are much more pronounced than in Fig. 3.11, indicating that the higher-order mode groups are fairly strongly excited. Use of such lasers makes the uniform distribution model more realistic.

Note that for very small parameters of the input fibers ( $a_1/a_0 \lesssim 0.5$ ) the geometrical optics approach gradually loses its validity, and so the results for the multiplexers in this region are less accurate.

### 3.2.4 Experimental Results

The fabrication of the butt-joint multiplexer is as follows [4]: About 3 cm of a graded index fiber, with core diameter  $33 \mu\text{m}$ , are glued into a glass capillary. Next, the embedded fiber is polished from a point of the circumference sloping towards its end. The polishing angle is  $1.5^\circ$ . The second polishing at the fiber endface is at right angles to the surface just obtained. Two of these multiplexer parts are aligned under a microscope using a micromanipulator, and are glued in such a way that the two ends have the geometry shown in Fig. 3.2. Finally, the output fiber with the polished endface is butt-joined to the composite unit thus obtained. In order to get a four-channel multiplexer, the fiber parts in the capillary have to be prepared once more in the manner described above, so that four quarters are obtained (see Fig. 3.4). The resulting multiplexer device is shown in the photograph in Fig. 3.13. It is a stable and rugged structure with small outer dimensions,  $9 \times 15 \times 55 \text{ mm}$ .

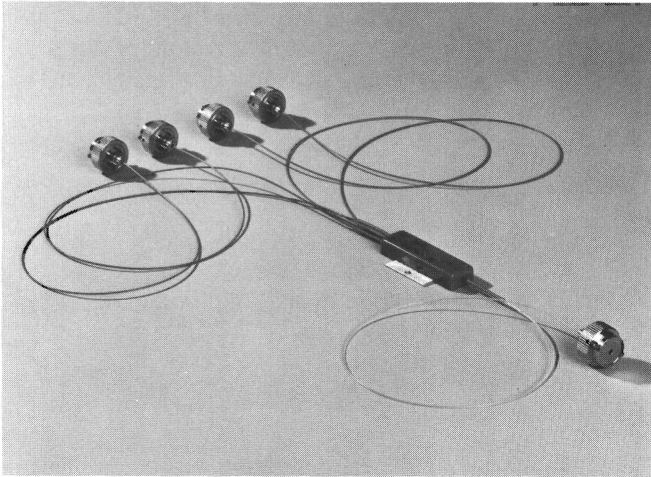


*Fig. 3.13 Photograph of a four-channel butt-joint multiplexer*

Furthermore, the fiber pigtails of the multiplexer are terminated with lens connectors.

Insertion losses of the butt-joint multiplexer were measured with a halogen lamp in combination with an interference filter ( $\lambda_0 = 850 \text{ nm}$ ,  $\Delta\lambda = 10 \text{ nm}$ ). The coupled light reaches the multiplexer after transmission through a 1.5 meter input fiber. Next, the light power transmitted through the output fiber was compared with the light power coupled to the input fiber, which was measured after cutting the input fiber in front of the multiplexer.

Ten samples of a two-channel multiplexer have been constructed. For each channel we measured an insertion loss within 0.6 – 0.8 dB. As the theoretical value for this multiplexer is 0.55 dB, it can be concluded that the agreement is quite satisfactory. The experimental values of several four-channel multiplexers are given in Table 3.3.

device	channel loss (dB)			
	1	2	3	4
I	2.3	1.9	1.5	1.3
II	1.6	1.4	2.3	2.4
III	1.6	2.0	1.2	1.6
IV	1.3	1.7	2.2	1.7

*Table 3.3 Experimental results of several four-channel multiplexers*

Here, the agreement is not as good as in the previous case. The reason for this is the increased difficulty of correct polishing, glueing and alignment in a four-channel structure.

### 3.3 Prism Multiplexer

#### 3.3.1 Theory

The optical arrangement of a two-channel prism multiplexer is shown in Fig. 3.14.

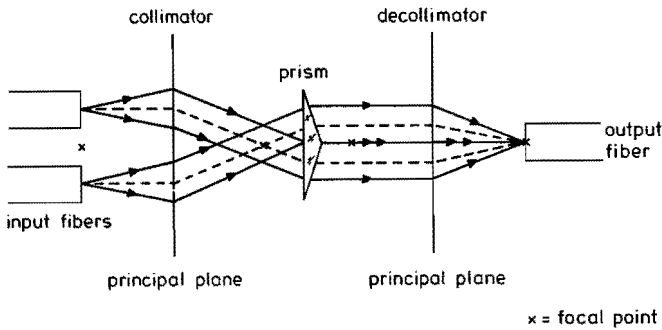


*Fig. 3.14 Optical arrangement of the prism multiplexer*

The input fibers are coupled to the output fiber by means of a collimator, roof prism and decollimator. The endfaces of the input fibers are located in the collimator focal plane. As the optical axes of the input fibers do not coincide with the axis of the lens system, the two nearly perfect collimated beams will form an angle with each other and with the optical axis. A prism is located at the point where the beam overlap is sufficiently small. Its refracting angle is chosen in such a way that both light beams are parallel with the optical axis after passing through the prism. Light in a possible beam overlap hits the wrong facet of the prism and makes no contribution to the coupling. Finally, both beams are focused at the endface of the output fiber, which is located in the focal plane of the decollimator on the optical axis of the lens system.

In this multiplexer the spatial filtering occurs between the collimator and decollimator. As we have pointed out in section 1.5, the light beams between the lenses can be conceived of as imaginary fibers. Just behind the prism we have a light pattern, which is equivalent to the cross-section at the junction of a butt-joint multiplexer shown in Fig. 3.2. For the determination of the insertion loss of prism multiplexers Eqs. (3.3) and (3.4) are still valid. In these equations  $a_1$  and  $a_0$  have to be replaced by the radius of the collimated input and output beams,  $f_1 \cdot NA_1$  and  $f_0 \cdot NA_0$ , respectively.

The prism multiplexers offer more freedom in design than the butt-joint multiplexer, because additionally the focal lengths of both lenses can be chosen arbitrarily. The structure can be extended to an arbitrary number of channels when using a prism with a number of facets corresponding to the number of channels. In Fig. 3.15 an impression is given of a four-channel multiplexer.

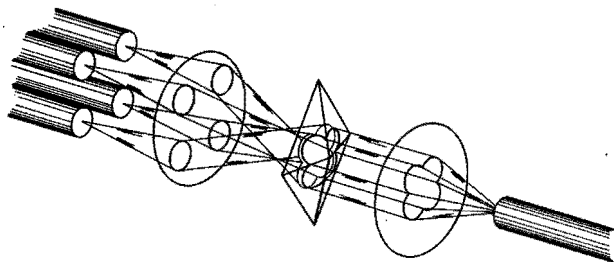


Fig. 3.15 Impression of a four-channel prism multiplexer

### 3.3.2 Design

The analysis starts with the calculation of the deviation angle for any ray traversing a prism. Refraction by a prism is shown in Fig. 3.16, where it has been assumed that the prism has a refracting angle  $\gamma$  while its index is  $n$ . The deviation angle  $\delta$  is calculated from

$$\delta = \varphi_1 - \gamma + \arcsin[n \sin \{ \gamma - \arcsin(n^{-1} \sin \varphi_1) \} ] \quad (3.46)$$

where  $\varphi_1$  is the angle of incidence.

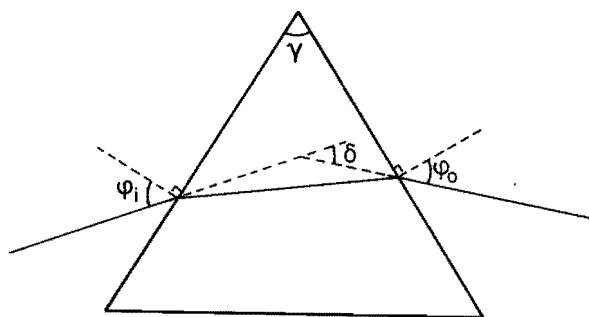


Fig. 3.16 Definition of ray angles in the refraction by a prism

When using Eq. (3.46) it turns out that  $\delta$  varies considerably with the angle of incidence  $\varphi_1$ . It is preferable to use prisms at minimum deviation because otherwise any slight divergence of the incident light would cause astigmatism in the image. Considering the prism configuration in Fig. 3.14 it follows that  $\gamma = \varphi_1 = \delta$ . In that case Eq. (3.46) reduces to

$$\gamma = \arcsin[n \sin\{\gamma - \arcsin(n^{-1} \sin\delta)\}] \quad (3.47)$$

Using some goniometric relations, Eq. (3.47) can be rewritten as

$$\tan\gamma = \frac{\sin\delta}{(n^2 - \sin^2\delta)^{1/2} - 1} \quad (3.48)$$

At minimum deviation it turns out that  $\varphi_1 = \varphi_0$  (see Fig. 3.16). In our configuration we then have

$$\sin\delta = n \sin(\gamma/2) \quad (3.49)$$

Substitution of Eq. (3.49) into Eq. (3.48) yields

$$n = 2\cos(\delta/2) \quad (3.50)$$

As we always have  $\delta \ll 1$ , it is required that  $n = 2$  to satisfy all conditions. On the other hand, for thin prisms ( $\gamma$  small) the following approximation is valid

$$\delta \cong (n - 1)\gamma \quad (3.51)$$

In Eq. (3.51) the angle of incidence is of no importance, so that the requirement  $n = 2$  is not so strong in practice.

To determine the refracting angle  $\gamma$  and the distance  $s$  between the back focal point and flat side of the prism we use the optical diagram shown in Fig. 3.17. The input

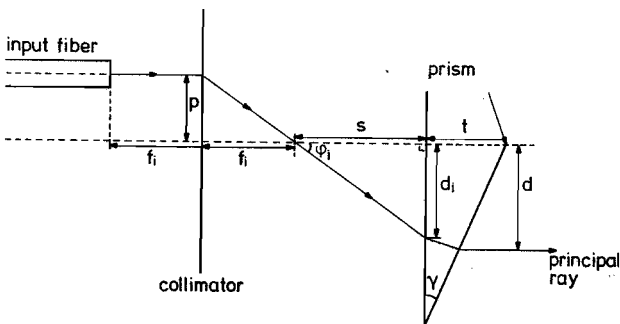


Fig. 3.17 Optical diagram for the design of a prism multiplexer

fibers are assumed to have an offset  $p$ . By elementary ray-tracing we see that the angle of incidence  $\varphi_i$ , which equals the deviation angle  $\delta$ , is given by

$$\delta = \varphi_i = \arctan(p/f_i) . \quad (3.52)$$

The value of the refracting angle  $\gamma$  is obtained by substituting Eq. (3.52) into Eq. (3.48).

Using Eqs. (3.3) and (3.4) we choose an appropriate value of  $d$ . The principal ray hits the flat side of the prism at a distance  $d_1$  from the axis:

$$d_1 = d - (t - d \cdot \tan\gamma) \tan\varphi_1 , \quad (3.53)$$

with

$$\varphi_1 = \arcsin(n^{-1} \sin\varphi_i) . \quad (3.54)$$

Finally the distance  $s$  is obtained from

$$s = d_1/\tan\varphi_1 . \quad (3.55)$$

### 3.3.3 Experimental Results

We have based the practical construction of the prism multiplexer on the lens connector described in chapter 1. It is stretched out axially to create space for optical processing elements between the lenses. The modified input plug incorporates an array of three fibers: two input fibers and a dummy in between. The central dummy fiber is used to align the plug to the optical axis according to the alignment procedure of Ref. 5. The two input fibers, whose signals should be multiplexed, are now located automatically at equal distances from the axis. At the output the fiber end is mounted in the usual lens plug. Finally, the prism is mounted in an adapter, which is provided with bayonet catches for the lens plugs. The parameters of the multiplexer parts listed in Table 3.4 have been chosen in accordance with the lines presented in section 3.3.2. A photograph of the device, with the prism in front of it, is shown in Fig. 3.18. The loss estimation is given in Table 3.5. Insertion losses were measured under uniform launching conditions. A small overlap of the beams did occur, resulting in a loss of 0.2 dB after Eqs. (3.3) and (3.4). The coupling between the alignment fiber at the input side and the output fiber, using only the two lens plugs, showed a loss of 0.3 dB, caused by lens aberrations. All surfaces were AR-coated, except those of the prism. This results in a loss of 0.35 dB. So, we are left with an additional loss of 0.6 dB due to tolerances in the multiplexer parts.

Using exact ray-tracing by standard methods we obtained numerically an insertion loss of 0.7 dB. This does not differ too greatly from the essential  $0.2 + 0.3 = 0.5$  dB loss, estimated in the experiment.

Finally, we note that perfect channel symmetry can easily be obtained by transverse adjustment of the prism.

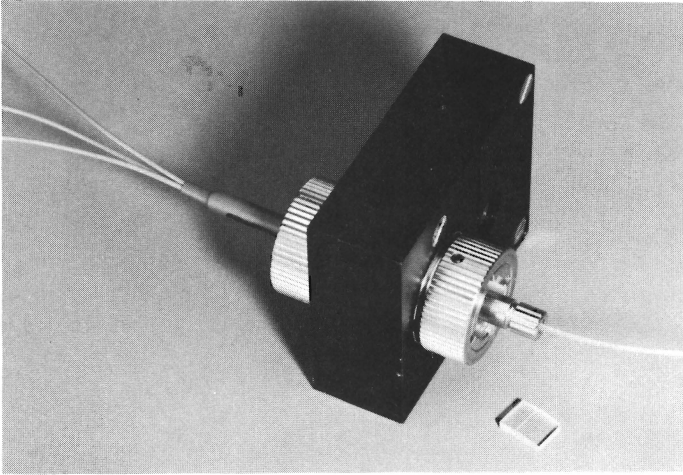


Fig. 3.18 Photograph of the multiplexer device, with the prism in front of it

Ball-lens parameters		
	collimating lens	decollimating lens
focal length	2.73 mm	3.86 mm
diameter	4.95 mm	7.00 mm
material	LASF 9	LASF 9
Fiber parameters		
	input fiber	output fiber
core diameter	33 $\mu\text{m}$	50 $\mu\text{m}$
cladding diameter	125 $\mu\text{m}$	125 $\mu\text{m}$
index profile	graded	graded
Prism parameters		
roof angle	167° 42'	
material	BK 7	
dimensions:		
base	8 x 6 mm	
height	2 mm	

Table 3.4 Parameters of multiplexer parts



<b>factors</b>	<b>losses</b>
<b>coupling input to output fiber</b>	<b>0.3 dB</b>
<b>beam overlap</b>	<b>0.2 dB</b>
<b>tolerances in multiplexer parts</b>	<b>0.6 dB</b>
<b>reflection losses</b>	<b>0.35 dB</b>
<b>total</b>	<b>1.45 dB</b>

*Table 3.5 Loss estimation of prism multiplexer*

## REFERENCES

1. E.G. Neumann and W. Weidhaas, AEU 30, 448 (1976).
2. M. Born and E. Wolf, Principles of Optics (Pergamon Press, Oxford, 1975), p. 122.
3. E.W. Marchand, Gradient Index Optics (Academic Press, New York, 1978), p. 59.
4. D. Opielka and D. Rittich, Electron. Lett. 15, 757 (1979).
5. A. Nicia, Electron. Lett. 14, 511 (1978).

## 4. DESIGN AND CONSTRUCTION OF OPTICAL DEMULTIPLEXERS

### 4.1 Introduction

In section 2.3 we have reviewed the principles of optical demultiplexers. It is expected that angular-dispersive devices have advantages in that insertion losses and the number of basic elements do not increase with the number of channels, as long as that number is not too large. Furthermore, it is possible to have closely spaced channels with low cross-talk and at the same time a flat pass band. These properties are hard to achieve with interference filters.

A demultiplexer with angular dispersion can advantageously be fabricated as an autocollimator in a Littrow mount with a single lens, a grating or prism, and an input-output fiber array. Owing to the desired small channel spacing ( $\sim 30$  nm) a blazed reflection grating is the best element for constructing compact demultiplexers. Prisms have such a low dispersion that miniaturization and the use of single-element lenses would not be possible.

### 4.2 Ball Lens Demultiplexer

#### 4.2.1 Theory

The device configuration is shown in Fig. 4.1. The signal from the input fiber is collimated by the ball lens, diffracted at different angles according to the wavelength on the grating surface, and the resulting beams are then focused on the corresponding output fiber by the same ball lens.

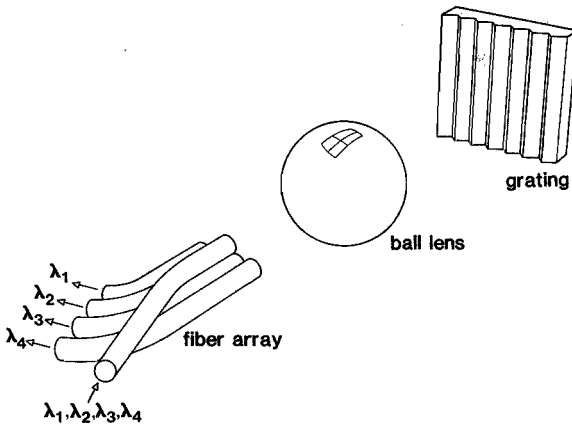


Fig. 4.1 Structure of demultiplexer based on Littrow mounting

Relations between the channel spacing, defined as the wavelength difference between adjacent channels, and the element parameters are derived in the following. A model for the derivation is shown in Fig. 4.2. A reflection grating with period  $\Lambda$  and blaze angle  $\theta_B$  is positioned in front of a ball lens. The normal of the grating plane forms an angle  $\theta$  with the optical axis, which is the line through the core center of the input fiber and the center of the ball lens.

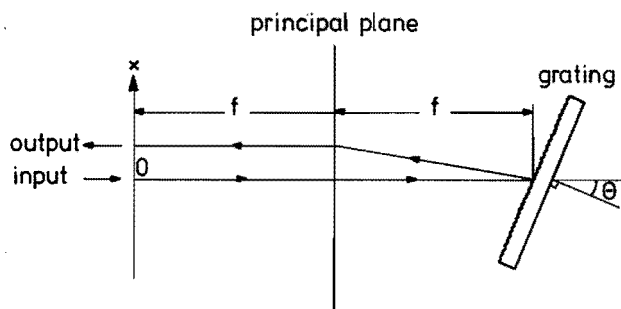


Fig. 4.2 Optical diagram for the design of a grating demultiplexer

The grating equation is described as [1]

$$m\lambda = \Lambda (\sin\alpha + \sin\beta) = 2\Lambda \sin\left(\frac{\alpha + \beta}{2}\right) \cos\left(\frac{\alpha - \beta}{2}\right), \quad (4.1)$$

where  $\alpha$  and  $\beta$  are incident and diffracted ray angles respectively, with respect to the normal of the grating plane,  $m$  is the diffraction order and  $\lambda$  is the wavelength. We will only consider the first order ( $m = 1$ ), because it is well-known that this order has the highest efficiency. For the Littrow mounting ( $\alpha = \beta = \theta$ ) Eq. (4.1) reduces to

$$\sin\theta = \lambda/(2\Lambda). \quad (4.2)$$

In reality there always will be a difference of some degrees between  $\alpha$  and  $\beta$ . For practical purposes, however, Eq. (4.2) remains valid. Under this condition the angular dispersion is given by

$$\frac{d\beta}{d\lambda} = \frac{2}{\lambda} \tan\theta. \quad (4.3)$$

To obtain the linear dispersion  $dx/d\lambda$  we have to multiply Eq. (4.3) by the focal length  $f$  of the ball lens [see also Eq. (2.5)].

The grating period  $\Lambda$  must be chosen such that the central wavelength  $\lambda_c$  of the

demultiplexer appears near autocollimation at the blaze angle  $\theta_B$ . This is desirable because the highest diffraction efficiency and its smallest polarization dependence are then expected [2]. Additional to a certain channel spacing we want to have a flat pass band characteristic, so that the demultiplexer can perform without loss changes against the emission wavelength variations in laser diodes. Such a flat pass band can be obtained by using oversized step-index output fibers. In the following we will discuss the choice of output fiber parameters.

For purely monochromatic light a nearly unbroadened image of the input fiber core cross-section appears in the focal plane, where the endface of the fiber array is located (see also Fig. 4.2). This image is considered to move on the output fiber cores as the emission wavelength changes. Therefore, the width of the flat pass band is determined by the linear dispersion and the difference in core diameter of input and output fibers. The explicit relation is

$$B = 2(a_0 - a_i)\Delta\lambda/D , \quad (4.4)$$

where

- B = bandwidth of flat pass band,
- $a_i$  = core radius of input fiber,
- $a_0$  = core radius of output fiber,
- D = distance between fiber axes of adjacent output fibers,
- $\Delta\lambda$  = channel spacing.

From Eq. (4.4) it will be clear that maximum bandwidth is obtained if  $a_0 \gg a_i$  and  $D \cong 2a_0$ . The latter requirement indicates that the cladding thickness of the output fibers should be as small as possible. A practical limit for this thickness seems to be  $20 \mu\text{m}$ . The sensitive area of high-speed photodiodes at the receiver end sets an upper limit of about  $50 \mu\text{m}$  on  $a_0$  [3]. As the input fiber is nearly always the standard graded-index fiber ( $a_i = 25 \mu\text{m}$ ) we have, according to Eq. (4.4), for the obtainable bandwidth

$$B_{\text{max}} = 0.35 \Delta\lambda . \quad (4.5)$$

Note that all fibers in the array should be located as closely as possible to the optical axis in order to reduce astigmatism of the ball lens.

When selecting components for a demultiplexer we have to know the acceptable bandwidth and an estimation of the groove spacing of the grating. The connection between all element parameters is shown in the flow chart in Fig. 4.3. It is pointed out that there is an interaction between focal length and groove spacing. For ball lenses the spherical aberration is proportional to  $f$ . Thus,  $f$  should be chosen in such a way that the image of the input fiber does not broaden to much. On the other

hand, as a general rule coarser gratings have higher efficiencies. In an actual design a compromise should be made between the above-mentioned effects.

The grating efficiency peak is always found around the Littrow angle. When a commercially available grating is used, its blaze angle should be chosen as close as possible to this Littrow angle.

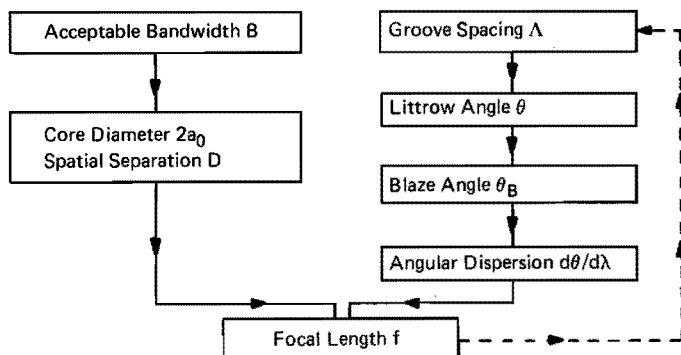


Fig. 4.3 Connection between element parameters in a grating demultiplexer

#### 4.2.2 Experimental Results

It is very convenient to start the design by making a selection table for a demultiplexer with a given central wavelength, number of channels, and so on. Table 4.1 shows such a table for a four-channel device in the 850 nm region. It is based on available ball lenses with diameters in the range of interest, fabricated from Schott glass LaSF9, and Bausch and Lomb standard gratings. For reasons pointed out in the previous section, we use step-index output fibers with parameters of 100  $\mu\text{m}$ /140  $\mu\text{m}$ . From the selection table we see that with these output fibers a good choice is

- grating : 1200 grooves/mm
- ball lens : diam. 9 mm
- linear separation : 205  $\mu\text{m}$ .

The complete demultiplexer is shown in the photograph in Fig. 4.4, and an end view of the fiber array can be seen in Fig. 4.5.

Grooves/mm	$\theta = \arcsin \left( \frac{\lambda_c}{2\Lambda} \right)$	Neighbouring Blaze Angle $\theta_B$	Grating Efficiency	$\Delta\theta = \frac{\Delta\lambda}{\lambda_c} 2 \tan \theta$	Linear Separation ( $\mu\text{m}$ )					
					$\phi 5$	$\phi 6$	$\phi 7$	$\phi 8$	$\phi 9$	$\phi 10$
1800	47°57'	26°45'	47%	80.6 mRAD	220					
1200	29°40'	36°50'	84%	41.4 mRAD	113	140	160	182	205	
1200		26°45'	76%							
830	20°1'	20°34'	85%	26.5 mRAD	72	88	102	117	131	146
800	14°20'	17°27'	76%	18.6 mRAD		61	72	82	92	102
600		13°	72%							

$$\lambda_c = 825 \text{ nm}$$

$$\Delta\lambda = 30 \text{ nm}$$

$$f = \frac{n}{2(n-1)} r = 1.102 r$$

$$n = 1.83$$

Table 4.1 Selection table for the design of a specified demultiplexer

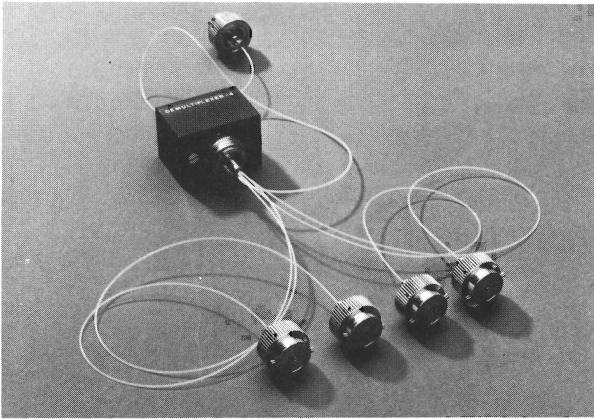


*Fig. 4.4 Photograph of grating demultiplexer*

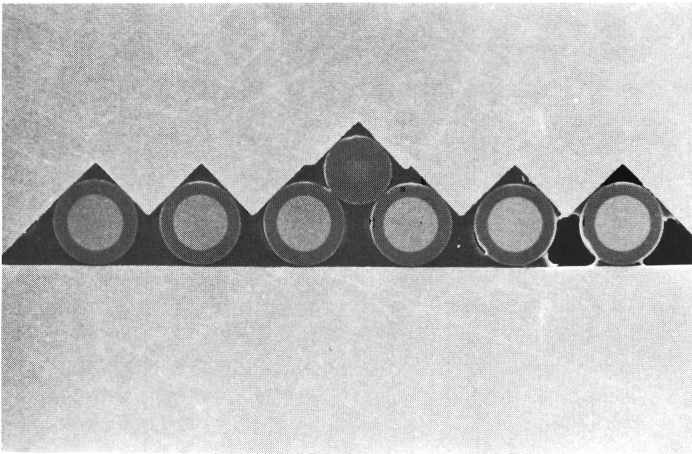


*Fig. 4.5 Micro photograph of fiber array*

Spectral transmission curves were measured using a halogen lamp in combination with a monochromator as light source. The spectral width was set at 0.1 nm. Absolute transmission curves were measured by comparing the power transmitted through each output fiber with the light coupled to the input fiber, which was measured by cutting the input fiber pigtail.

We also calculated the pass bands using numerical integration and ray-tracing. Fig. 4.6 shows calculated (drawn lines) and experimental (marks) results. The output of each channel corresponds to one of the output fibers. The insertion loss in the pass bands is 1.2 – 1.3 dB, which is mainly caused by the grating (~1 dB). The residual loss originates from Fresnel reflection at the fiber endfaces in the array.

The calculations show that there is no lens coupling loss in the flat pass band. That is why we have matched experimental and numerical data in this region. It can be concluded that there is excellent agreement between numerical and experimental pass bands.

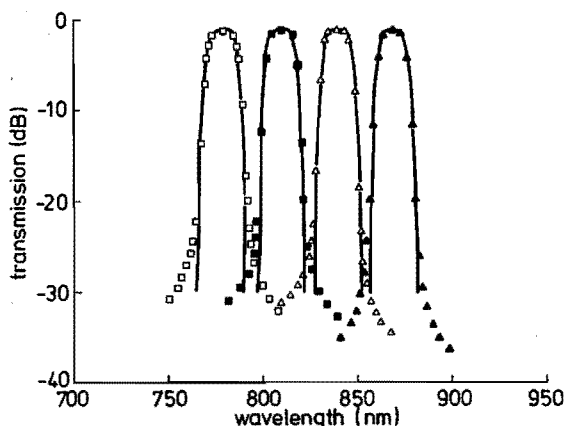


Fig. 4.6 Branching characteristic of a four-channel demultiplexer with anti-reflection coated ball lens. (The marks are the experimental values.)

A proper anti-reflection coating on the ball lens is very important, because a possible reflection of the input fiber light is immediately directed towards both central output fibers. This light is not diffracted at the grating, so it will cause cross-talk in the central channels. If the front surface of the ball lens is thought of as a perfect mirror, then the input fiber couples 4.7% of its power to each of the inner output fibers of the array.

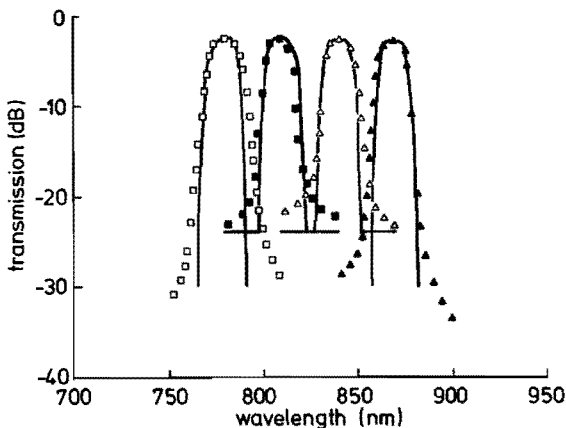
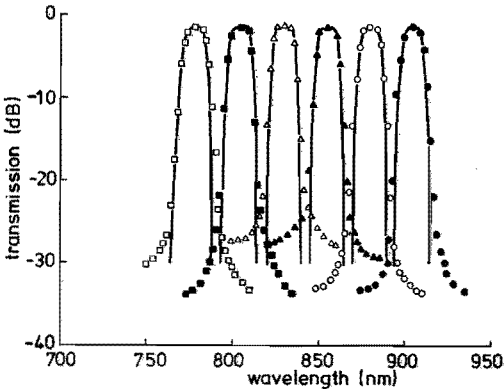


Fig. 4.7 Branching characteristic of a four-channel demultiplexer with an uncoated ball lens

To visualize this effect, we repeated the experiment with an uncoated ball lens. The reflection at the boundary is 8.6%, resulting in a direct coupling of  $4.7 \times 0.086 = 0.4\%$ , which corresponds to  $-24$  dB. Taking this effect into account, we obtain the results shown in Fig. 4.7.

Finally, we have also constructed a six-channel demultiplexer. Its experimental and numerical characteristics are shown in Fig. 4.8. The insertion loss in the flat pass band is  $1.4 - 1.6$  dB, which is only a slight increase as compared with the four-channel version.



*Fig. 4.8 Branching characteristic of a six-channel demultiplexer with anti-reflection coated ball lens*

### 4.3 Linear Polarization Demultiplexer

In the experiments it turned out that insertion losses are mainly caused by the grating. However, the technology of fabricating gratings has reached its theoretical limits, and therefore no improvements in the structure shown in Fig. 4.1, are to be expected. If we use polarization effects in the diffraction at the grating, then there is a possibility of reducing insertion losses reported in the previous section. To explain this, we have to consider the behavior of blazed gratings, which is mainly determined by the blaze angle.

From the grating point of view it would be desirable to insert only gratings of the very low blaze angle region ( $1 - 5^\circ$ ). Polarization effects are then negligible, and the efficiency peaks towards almost 100%. However, such gratings require a large focal length in the demultiplexer, preventing miniaturization. Outside this very low blaze angle region the efficiency curves for the P- and S-planes (electric field vector parallel (P) and perpendicular (S) to the grooves) are always remarkably different. A survey of all blaze angles shows that in the high blaze angle region ( $22 - 38^\circ$ )



the S-plane efficiency is very high and wide-band. In Fig. 4.9 we show the characteristics of a standard grating in this high blaze angle region [2].

Fig. 4.9 indicates that we can get better demultiplexers if the light is linearly polarized just before impinging upon the grating. For a loss-free transfer of unpolarized light into linear polarized light we need two subfunctions: (a) spatial decomposition of the unpolarized light beams into two linear polarized light beams, and (b) rotation of the electric field vector of one of the beams just obtained into the direction of the field vector of the other beam. The first function can be realized by using polarizing interference filters or uniaxial crystals. Rotation of the field vector is achieved by half-wave retarders.

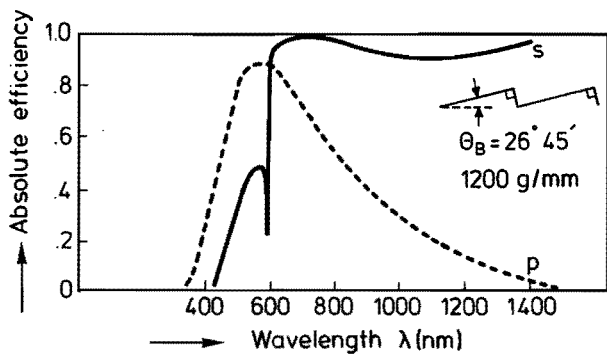


Fig. 4.9 Characteristics of a standard grating at Littrow condition

A suggested approach is shown in Fig. 4.10. It is the usual concept of a grating demultiplexer with a so-called linearizer inserted between the ball lens and grating. When the collimated beam is sent into the prism it is reflected or transmitted according to its polarization by a multilayer interference filter. After the total

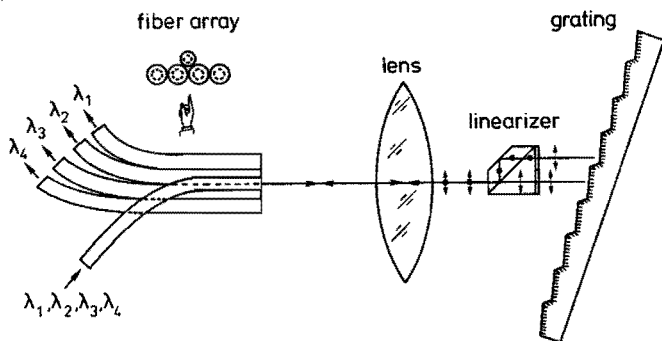


Fig. 4.10 Grating demultiplexer with linearizer inserted

internal reflection we have two parallel beams with perpendicular polarization, as indicated by circles or arrows in the figure. The half-wave plate, placed in the upper beam, rotates the field vector through  $90^\circ$ . The two separated beams thus emerge from the prism with the same direction of polarization, and are diffracted at the grating. After diffraction the linearizer is used in the opposite direction to combine both diffracted beams.

## REFERENCES

1. F.A. Jenkins and H.E. White, *Fundamentals of Optics* (McGraw-Hill, New York, 1976), p. 360.
2. E.G. Loewen et al., *Appl. Opt.* 16, 2711 (1977).
3. D.P. Schinke et al., *Photodetectors, in Semiconductor Devices for Optical Communication*, H. Kressel, Ed. (Springer Verlag, Berlin, 1980), pp. 63 – 87.

## SUMMARY AND CONCLUSIONS

The basic structure of most fiber-optical devices can be reduced to a centered imaging system with a collimating and a focusing lens. These devices always exhibit optical coupling loss, which is completely determined by the degree to which the optics depart from ideal, that is, by the aberrations and misalignments of the elements incorporated. A systematic approach is presented to predict the coupling efficiency for a specified set of lens and fiber parameters.

GRIN-rod lenses, ball lenses, and plano-convex rod lenses are currently proposed for fiber-optical devices. From analyses of the aberrations of these lens types it turned out that equivalent lenses in a well-designed coupling cause almost the same loss due to aberrations. Results of this theory are used to design a lens connector fabricated in a factory-type production line. Its performance reaches the theoretical limit. With the usual graded-index fibers this resulted in a mean value of 0.7 dB of the insertion loss.

Optical multiplexers and demultiplexers are indispensable in systems using wavelength division multiplexing (WDM). Because of the importance of WDM, optical (de)multiplexers have been investigated in this thesis. The analysis starts at the optimizing of the transmitter end (laser-fiber coupling + multiplexer) of a WDM system. To include all types of laser diodes, the current laser-fiber coupling theory is extended to include astigmatic laser diodes. Also, some fundamental limits as regards the efficiency of multiplexers without dispersive elements are derived. The choice between wavelength-selective and wavelength-independent multiplexers is discussed. The combination of index-guided laser diodes and wavelength-independent multiplexers is shown to be the best one for WDM systems, whereas it is preferable for multiplexing of LED signals to be done by means of wavelength-selective devices. Two novel types of wavelength-independent multiplexers are presented: a structure without lenses, which we name butt-joint multiplexer, and a structure using lenses, referred to as a prism multiplexer. Loss estimations showed that the insertion loss of the butt-joint multiplexer can hardly be reduced. However, the excess loss of the prism multiplexer, coming to 0.6 dB, is due to fabrication tolerances.

Finally, several grating demultiplexers have been constructed. The measured insertion losses in the pass bands were entirely determined by the grating efficiency ( $\sim 1$  dB). Furthermore, the cross-talk levels obtained were sufficiently low to satisfy all nowadays system requirements.

## SAMENVATTING EN CONCLUSIES

De basisstructuur van de meeste optische componenten voor glasvezels kan worden herleid tot een gecentreerd afbeeldingssysteem met een collimator en een decollimator. Deze componenten vertonen altijd een optisch koppelverlies dat volledig wordt bepaald door de onvolmaaktheid in het samenstel van de optische bouwstenen, te weten, afbeeldingsfouten en afwijkingen in de positionering. Er wordt een systematische aanpak opgesteld om voor een gegeven combinatie van lens- en glasvezelparameters een voorspelling van het koppelrendement te kunnen maken.

In optische componenten voor glasvezels worden meestal staaflenzen met een gegradeerde index, bollenzen, of platbolle staaflenzen gebruikt. Analyse van de afbeeldingsfouten van deze soorten lenzen toont aan dat in een goed ontworpen koppeling equivalente lenzen nagenoeg hetzelfde koppelrendement mogelijk maken. De resultaten van deze theorie zijn toegepast in het ontwerp van een lensconnector, die onder produktieomstandigheden wordt vervaardigd. De eigenschappen van de connector benaderen de theoretische grenzen. Voor de gebruikelijke gegradeerde index vezel betekent dit een gemiddeld verlies van 0,7 dB.

Optische multiplexers en demultiplexers zijn onmisbaar in systemen waarin golflengtemultiplex (WDM) wordt toegepast. Vanwege het belang van WDM worden in dit proefschrift optische (de)multiplexers onderzocht. Begonnen wordt met de optimalisatie van het zendergedeelte (laser-vezel koppeling + multiplexer) van een WDM-systeem. Om alle soorten laserdiodes te kunnen toepassen, was het noodzakelijk om de bestaande koppeltheorie uit te breiden met astigmatische laserdiodes. Verder worden er enkele fundamentele grenzen ten aanzien van het rendement van multiplexers zonder dispersieve elementen afgeleid.

De keuze tussen golflengte-selectieve en golflengte-onafhankelijke multiplexers wordt besproken. Het blijkt dat de combinatie van index-geleide lasers en golflengte-onafhankelijke multiplexers het beste is, terwijl het multiplexen van LED-signalen bij voorkeur dient te gebeuren met golflengte-selectieve multiplexers. Twee nieuwe typen multiplexers worden voorgesteld: een zonder lenzen, die we direct-contact multiplexer noemen, en een die we aanduiden als prisma-multiplexer.

Analyse van de verliezen maakt duidelijk dat de kwaliteit van de direct-contact multiplexer nauwelijks kan worden verbeterd. Daarentegen zijn de maakverliezen (0,6 dB) in de prisma-multiplexer aan de hoge kant.

Tenslotte zijn er ook nog diverse tralie-demultiplexers gerealiseerd. De in de doorlaatbanden gemeten verliezen worden volledig bepaald door het rendement van het gebruikte tralie ( $\sim 1$  dB). Verder zijn de verkregen overspraakniveaus ruimschoots voldoende om aan alle huidige systeemeisen te kunnen voldoen.

## CURRICULUM VITAE

De schrijver van dit proefschrift werd op 25 juli 1950 geboren te Breda, waar hij in 1971 met lof het eindexamen in de afdeling Elektrotechniek van de Hogere Technische School aflegde. In hetzelfde jaar begon hij met zijn studie Elektrotechniek aan de Technische Hogeschool Delft. In augustus 1975 studeerde hij af, met lof, bij prof. dr. ir. A.T. de Hoop.

Sinds oktober 1975 is de auteur werkzaam als wetenschappelijk medewerker bij het Philips Natuurkundig Laboratorium te Eindhoven. Het in dit proefschrift beschreven werk werd verricht in de groep *Wideband Communication Systems* onder leiding van ir. J.H.C. van Heuven.

Stellingen bij het proefschrift:

MICRO-OPTICAL DEVICES FOR  
FIBER COMMUNICATION

1. De beschrijving die Simon e.a. geven van het ontdekken van fysische en chemische wetten door het computerprogramma BACON, is gebaseerd op de veronderstelling dat alle grootheden waarover het programma informatie dient te krijgen, relevant zijn voor het probleem. Bij het ontdekken van nieuwe wetmatigheden wordt aan deze veronderstelling zelden of nooit voldaan.  
  
- H.A. Simon, P.W. Langley, and G.L. Bradshaw, *Synthese* 47 (1981) 1
2. Bij de bepaling van de modusdispersie van een glasvezel volgens de snij-en-metmethode kunnen de resultaten onjuist of zelfs onzinnig worden, indien er merkbare kleurdispersie optreedt.
3. Grau en Lemminger beweren dat de door hen afgeleide relatie tussen de verre-veldintensiteit enerzijds en de vermogensverdeling van modi anderzijds geldig is voor glasvezels met een willekeurig brekingsindexverloop. De relatie is echter alleen geldig indien de brekingsindex wordt beschreven door een monotoon niet-stijgende functie.  
  
- G.K. Grau and O.G. Lemminger, *Appl. Opt.* 20 (1981) 457
4. De aantrekkelijkste methode voor het lassen van mono-modusglasvezels is die methode, waarbij door middel van lokale in- en uitkoppeling van licht het koppelrendement wordt gemeten.
5. Funakoshi e.a. kunnen dank zij onjuiste veronderstellingen in hun diffusiemodel de waargenomen tijd voor het vlakgroeien met vloeistoffase-epitaxie over een gegroefd GaAs-substraat verklaren.  
  
- K. Funakoshi, A. Doi, K. Aiki and R. Ito, *Journal of Crystal Growth* 45 (1978) 252

6. Bij het filteren van een verruist harmonisch signaal met behulp van een fasevergrendel-lus gaat men vaak uit van de onjuiste veronderstelling dat het vermogensspectrum van de ruis wordt gewogen met het kwadraat van het amplitudespectrum van de lus.

7. Gezien de eigenschappen van materialen voor thermomagnetische registratie is de benaming "amorf" voor structuurloze vaste stoffen ontoereikend.

- J.W.M. Biesterbos, Journal de Physique, 40  
(1979) C5-274

8. De gangbare beschrijving van de afgeschernde magnetische lusantenne leidt tot een verkeerd begrip en in berekeningen tot een veel te grote antenne-impedantie in het gebruikelijke meetgebied.

- H.W. Ott, Noise Reduction Techniques in Electronic Systems, John Wiley New York, 1976, p.48

- A. Hock, Hochfrequenzmesstechnik 1, Kontakt + Studium Lexika band 31, Technische Akademie Esslingen, Lexika Verlag 7031, 1979, p.229

9. Door een toevallige keuze van de hypotheekbedragen in de tarieftabel voor hypotheekaktes is een mogelijke dubbelzinnigheid in de bepaling van het hypotheekbedrag, behorend bij een gewenst te financieren bedrag, vermeden.

10. De belangrijkste reden om multi-modusglasvezel te gebruiken in hoogwaardige transmissiesystemen is de, als gevolg van de kleine kern, slechte hanteerbaarheid van de mono-modusvezel. Dit nadeel is echter van voorbijgaande aard.